Cyclic Deformation and Fatigue Damage Behavior of Cu Monocrystals, Bicrystals and Tricrystals

Zhongguang WANG†, *Xiaowu LI, Zhefeng ZHANG, Weiping JIA and Shouxin LI*
State Key Laboratory for Fatigue and Fracture of Materials, Institute of Metal Research, Chinese Academy of Sciences, Shenyang 110015, China

[Manuscript received May 13, 1999, in revised form May 24, 1999]

In the present work, the cyclic deformation behavior of Cu single crystals oriented for double- and multiple slip as well as Cu bicrystals and tricrystals was investigated under constant plastic strain control at room temperature in air. The main objectives of the study are: (1) to find out the effects of crystallographic orientation and grain boundary (GB) on the cyclic stress-strain (CSS) curves; (2) to compare the cyclic deformation behavior of the double-, multiple-slip crystals, bicrystals and tricrystals with that of single-slip oriented crystals and to correlate the results with those of polycrystals; (3) to examine the corresponding dislocation structures; (4) to investigate the interactions of persistent slip bands (PSBs) with GBs and triple joint (TJ) as well as intergranular fatigue cracking in Cu bicrystals and tricrystals.

1. Introduction

Most of mechanistic studies on cyclic deformation have been carried out on Cu crystals in single-slip orientations. There are several excellent review articles which emphasized different aspects of the subject[1~6]. When a well-annealed Cu crystal suitably oriented for single slip is subjected to cyclic deformation between constant plastic strain amplitude limits γ_{pl} at room temperature in air, it will harden under the action of cyclic straining. The peak stress increases rapidly at first and then more slowly, approaching a value, the saturation stress τ_s. A plot of saturation stress τ_s *vs* the plastic strain amplitude γ_{pl} generates the "cyclic stress-strain (CSS) curve". Mughrabi[7] performed constant plastic strain amplitude tests on single-slip oriented Cu single crystals over a wide range of amplitudes and obtained a well-documented cyclic stress-strain curve which clearly demonstrates three regions marked by A, B and C. At low values of plastic strain amplitude [$\gamma_{pl} \leq \gamma_{pl,M} = 6 \times 10^{-5}$], denoted region A, work hardening occurs during cyclic loading. Region A is followed by a strain-independent region B known as the "plateau". The plateau region extends over two decades of plastic strain amplitudes ($6\times10^{-5} < \gamma_{pl} < 7.5 \times 10^{-3}$). A further increase in plastic strain amplitude ($\gamma_{pl} > 7.5\times10^{-3}$) results in an increase in the saturation stress, which is region C. One of the most visible features of cyclic saturation is the formation of the highly localized and largely reversible slip bands, persistent slip bands (PSBs), which frequently act as preferential sites for fatigue crack nucleation. The plateau region B is characterized by the formation of the first PSBs at its lower end ($\gamma_{pl}=6\times10^{-5}$) and by the complete filling of the specimen volume with PSBs at its upper end ($\gamma_{pl}=7.5\times10^{-3}$). In the plateau region, τ_s remains essentially constant ($\approx$28 MPa) due to the localized cyclic deformation in the PSBs.

The dislocation structure in cyclically deformed Cu single crystals oriented for single slip is well known to strongly depend upon the applied amplitude (for example, see literatures [1~6]). In the plateau region, dislocation configuration can be described as "two-phase" structures: ladders and veins[8,9]. The ladder structure, corresponding to surface PSBs, is soft and carries most of the applied plastic strain, while the vein structure is hard and contributes little to cyclic deformation. At γ_{pl} below the lower end of the plateau, the dislocation structure consists only of veins. Finally, at γ_{pl} near the upper end of the plateau or beyond the plateau, labyrinth and cell structures which are associated with multiple slip may develop.

Compared with single crystals, our knowledge about the cyclic deformation mechanism in Cu polycrystals is obviously much less. As for polycrystalline materials, there are at least three distinct important features that bring about their deformation behavior in a manner very different from single crystal oriented for single slip: (1) many grains in a polycrystal will be in all kinds of double- or multiple-slip orientations, (2) grain boundaries (GBs) with different orientations and structures will act as obstacle against slip deformation and act as fatigue crack nucleation sites and,

† To whom correspondence should be addressed
Invited paper
E-mail: zhgwang@imr.ac.cn

furthermore, (3) due to elastic as well as plastic deformation incompatibility between adjacent grains, it seems that all the grains in a polycrystalline sample are always subjected to an actual multiaxial loading condition. Numerous studies on polycrystalline materials have also been carried out in a similar method to that need for studying single crystals. One of the purposes of such studies is to correlate the results from single crystal studies with those for polycrystals. However, a direct application of the results obtained from single-slip crystals to polycrystal behavior has been not satisfactory[10~14]. Obviously, study of the cyclic deformation behavior of double and/or multiple slip oriented single crystals as well as bicrystals and tricrystals has become more important as a route to correlate single crystal behavior with polycrystal behavior. However, results in this area are rather limited.

In the present work, systematic study of the cyclic deformation behavior of Cu single crystals oriented for double or multiple slip, Cu bicrystals with either parallel, perpendicular or tilting GBs has been carried out over a wide range of plastic strain amplitudes. Both the cyclic deformation response and the microstructures were investigated. The main objectives of the study are: (1) to establish the CSS curve and to find out the effects of crystallographic orientation and grain boundary, (2) to compare the cyclic deformation behavior of the double-, multiple-slip crystals, bicrystals and tricrystals with that of single-slip oriented crystals and to correlate the results with those of polycrystals, (3) to investigate and examine the corresponding dislocation structures and interactions between dislocations of different slip systems, (4) to investigate the interaction of PSBs with GBs and TJs and (5) to examine the intergranular fatigue cracking in Cu bicrystals and tricrystals.

2. Cyclic Deformation Behavior of Cu Single Crystals Oriented for Double or Multiple Slip

Cheng and Laird[15] measured the cyclic saturation stresses of Cu crystals with a very wide variety of orientations inside the stereographic triangle, including some near to its boundaries. All crystals saturated remarkably near 29 MPa. Cheng and Laird therefore concluded that the cyclic saturation stress is independent of orientation. However, in the case of double- or multiple-slip-oriented Cu single crystals where two or more slip systems are simultaneously excited, rather different cyclic deformation behavior has been investigated. Kemsley and Paterson[16] investigated cyclic hardening of Cu crystals with various orientations. They found that [001] and [$\bar{1}$11] Cu crystals oriented for multiple slip hardened much more rapidly than single slip crystals in the total strain amplitude range from 5×10^{-4} to 2.5×10^{-3}. Lepisto and Kettunen[17] also examined the cyclic stress-strain behavior of [$\bar{1}$11] Cu crystals at strain amplitudes between 3×10^{-4} and 2.5×10^{-3}. Except for a higher initial cyclic hardening rate, they again found that the saturation behavior was not quite clear for this orientation. The resolved shear stresses at the end of tests were found to change from 36.2 to 60.9 MPa. A relatively more systematic work was carried out by Jin and Winter[18~21] who studied cyclic response and dislocation structures of Cu single crystals oriented for double and multiple slip at one single strain amplitude ($\gamma_{pl} = 3 \times 10^{-3}$). They reported that the initial cyclic hardening rates of [$\bar{1}$12], [012] and [$\bar{1}$22] double slip oriented crystals were, respectively, higher than, similar to and lower than that of the single slip crystal, while the saturation shear stresses were found to be 28.3, 31.4 and 35.8 MPa, respectively, compared with 29.7 MPa for the single slip crystal. The [001] crystals showed a much higher cyclic hardening rate than the other crystals and also a higher saturation stress of 44.0-46.9 MPa. However, no clear CSS curves and the associated microstructures for double- and multiple-slip-oriented Cu crystals have been reported.

2.1 Preparation of specimens and experimental procedures

Copper single crystal bars or plates were grown from OFHC Cu of 99.999% purity by the Czochralski or Bridgman method. A group of fatigue specimens oriented typically as [$\bar{1}$17], [$\bar{1}$12], [$\bar{2}$23], [017], [034], [$\bar{2}$55] and [$\bar{2}$33] for double slip and [001] and [011] for multiple slip were carefully spark machined from the as-grown single crystals. Three single-slip oriented crystals [$\bar{1}$35], [$\bar{1}$25] and [$\bar{4}$ 18 41] were also selected for comparison. The orientation of the specimens was determined by the Laue back-reflection technique with an accuracy of 2° in the crystal orientation. All the crystallographic orientations selected for the present study are shown in the standard stereographic triangle as indicated in Fig.1. It can be seen that [$\bar{1}$17], [$\bar{1}$12] and [$\bar{2}$23] on the 001/$\bar{1}$11 side, [017] and [034] on the 001/011 side, [$\bar{2}$55] and [$\bar{2}$33] on the 011/$\bar{1}$11 side

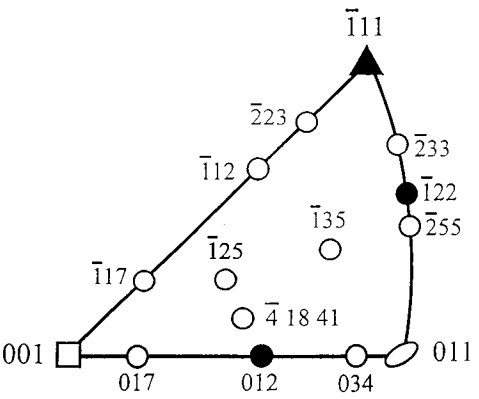

Fig.1 Crystallographic orientations of the fatigue specimens studied in the present work are indicated by open symbols. The solid dark symbols represent crystals studied by others[17,18]

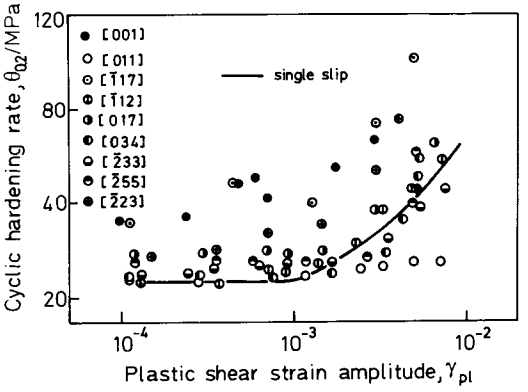

Fig.2 Initial cyclic hardening rate ($\theta_{0.2}$) *vs* plastic resolved shear strain amplitude (γ_{pl}) for double- and multiple-slip-orientation crystals. The solid line represents the results of single-slip-oriented crystals

are of the orientation types of conjugate, critical and coplanar slip, respectively. [001] and [011] are typical multiple slip orientations. Before fatigue testing, the specimens were annealed in vacuum at 800°C for 2 h and then electro-polished to remove surface strain and produce a mirror-like surface for microscopic observation.

Push-pull fatigue tests under plastic strain control were performed at room temperature in air using servo-hydraulic machines. A triangular waveform signal with a frequency of 0.05~0.5 Hz was usually adopted. Hysteresis loops were plotted by an X-Y recorder or recorded by a personal computer. All specimens were tested until the occurrence of cyclic saturation. After the fatigue tests, the specimen surface slip morphologies and interior microstructures were carefully observed by optical microscopy, scanning electron microscopy (SEM) and transmission electron microscopy (TEM), respectively. The cyclic straining induced dislocation configurations beneath the specimen surface were also examined by electron channeling contrast (ECC) technique in SEM.

2.2 Effect of crystallographic orientation on initial cyclic hardening rate[22~28]

The plot of $\theta_{0.2}$ against γ_{pl} was often used to measure the initial cyclic hardening rate[7]. $\theta_{0.2}$ is the mean initial cyclic hardening coefficient evaluated with the equation $\theta_{0.2} = \Delta\tau/\Delta\gamma_{pl,cum}$ at $\Delta\gamma_{pl,cum} = 0.2$, where $\Delta\gamma_{pl,cum}$ is the cumulative plastic strain, *i.e.* $\Delta\gamma_{pl,cum} = 4N\gamma_{pl}$ (N is the number of cycles proceeded and γ_{pl} is the plastic shear strain amplitude). The variation of $\theta_{0.2}$ with γ_{pl} for seven double slip oriented crystals and two multiple slip oriented crystals is given in Fig.2. Results for single slip oriented Cu single crystals are also given schematically in the same figure by a solid line for comparison.

Mughrabi[7] classified the cyclic hardening range into regimes I′ and II′ in the curve of $\theta_{0.2} - \gamma_{pl}$ for single slip crystals by taking a transition $\gamma_{pl} \approx 10^{-3}$. When γ_{pl} is below 10^{-3} (regime I′), $\theta_{0.2}$ is lower and almost independent of γ_{pl}. In the regime II′ where γ_{pl} is above 10^{-3}, $\theta_{0.2}$ increases notably with increasing γ_{pl}. It is interesting to note that the initial cyclic hardening rate is strongly affected by the crystallographic orientation. The curves of $\theta_{0.2} - \gamma_{pl}$ plotted in Fig.2 can be divided into three groups: (1) $\theta_{0.2}$ is lower and exhibits almost no change with increasing γ_{pl}. There is no two regimes in the $\theta_{0.2} - \gamma_{pl}$ curve, such as crystal [011], (2) $\theta_{0.2}$ is higher and increases continuously with increasing γ_{pl}. There is also no two regimes in the $\theta_{0.2} - \gamma_{pl}$ curve, such as crystals [$\bar{2}$23], [$\bar{1}$17] and [001], and (3) similar to single slip oriented crystals, the $\theta_{0.2} - \gamma_{pl}$ curves can be clearly divided into two regimes, such as crystals [$\bar{1}$12], [017], [034], [$\bar{2}$33] and [$\bar{2}$55].

The observed differences in $\theta_{0.2} - \gamma_{pl}$ curves of various crystals are closely related to the dislocation interactions between different slip systems. In Table 1 are listed the primary, conjugate, critical, cross slip and coplanar slip systems and their Schmid factors for double slip oriented crystals [$\bar{1}$17], [$\bar{1}$12], [$\bar{2}$23], [017], [034], [$\bar{2}$55] and [$\bar{2}$33]. $Q(=\Omega/\Omega_{max})$ is a geometrical parameter reflecting the possibility of the secondary slip system to be operated. It is generally accepted that the secondary slip system may operate when Q is larger than 0.9[15]. For [$\bar{1}$17] and [$\bar{2}$23] crystals lying on the 001/$\bar{1}$11 boundary of the standard orientation triangle, the reaction between primary and conjugate dislocations is essential and produces Lomer-Cottrell locks, a strong obstruction to dislocation movement. Therefore, higher $\theta_{0.2}$ values and a continuous increase in $\theta_{0.2}$ with γ_{pl} are expected for both [$\bar{1}$17] and [$\bar{2}$23] crystals as seen in Fig.2. On the middle of the 001/$\bar{1}$11 boundary is located [$\bar{1}$12] orientation which has almost no choice for cross-slip, but more possibility for co-planar slip. As indicated by the experiment results in Fig.2, [$\bar{1}$12] crystal behaves like a single slip crystal in the initial cyclic hardening although Lomer-Cottrell locks may also form in this crystal. As to other double slip crystals [017], [034], [$\bar{2}$55] and [$\bar{2}$33], the most effective reactions take place either between primary and critical dislocations or between primary and coplanar dislocations, giving up to sessile jogs or coplanar dislocations. They are weak obstructions to dislocation movement. Therefore, critical and coplanar double slip crystals usually show relatively lower initial cyclic hardening rate and two regimes in their $\theta_{0.2} - \gamma_{pl}$ curves, as seen for single slip crystals (Fig.2).

As can be seen in Fig.2, the initial cyclic hardening behavior is quite different between [001] and [011] crystals although both are oriented for multiple slip. This difference in the initial hardening rate should certainly be again attributed to the dislocation reactions between different slip systems. Theoretically, eight slip systems may operate simultaneously when

Table 1 Favored slip systems and relevant Schmid factors

Orientation	Slip system	Schmid factor, Ω	$Q=\Omega/\Omega_{max}$
$[\bar{1}17]$	primary slip $(111)[\bar{1}01]$	0.488	1
	conjugate slip $(\bar{1}\bar{1}1)[011]$	0.488	1
	critical slip $(\bar{1}11)[101]$	0.432	0.96
	cross slip $(1\bar{1}1)[\bar{1}01]$	0.320	0.71
	coplanar slip $(111)[1\bar{1}0]$	0.112	0.23
$[\bar{1}12]$	primary slip $(111)[\bar{1}01]$	0.408	1
	conjugate slip $(\bar{1}\bar{1}1)[011]$	0.408	1
	critical slip $(\bar{1}11)[101]$	0.272	0.67
	cross slip $(1\bar{1}1)[\bar{1}01]$	0	0
	coplanar slip (111) $[1\bar{1}0]$	0.272	0.67
$[\bar{2}23]$	primary slip $(111)[\bar{1}01]$	0.360	1
	conjugate slip $(\bar{1}\bar{1}1)[011]$	0.360	1
	critical slip $(\bar{1}11)[101]$	0.168	0.47
	cross slip $(1\bar{1}1)[\bar{1}01]$	0.120	0.33
	coplanar slip (111) $[1\bar{1}0]$	0.288	0.80
[017]	primary slip $(111)[\bar{1}01]$	0.457	1
	critical slip $(\bar{1}11)[101]$	0.457	1
	conjugate slip $(\bar{1}\bar{1}1)[011]$	0.392	0.86
	cross slip $(1\bar{1}1)[\bar{1}01]$	0.343	0.75
	coplanar slip (111) $[1\bar{1}0]$	0.065	0.14
[034]	primary slip $(111)[\bar{1}01]$	0.457	1
	critical slip $(\bar{1}11)[101]$	0.457	1
	conjugate slip $(\bar{1}\bar{1}1)[011]$	0.114	0.25
	cross slip $(1\bar{1}1)[\bar{1}01]$	0.065	0.14
	coplanar slip (111) $[1\bar{1}0]$	0.343	0.75
$[\bar{2}55]$	primary slip $(111)[\bar{1}01]$	0.423	1
	coplanar slip (111) $[1\bar{1}0]$	0.423	1
	conjugate slip $(\bar{1}\bar{1}1)[011]$	0.151	0.36
	cross slip $(1\bar{1}1)[\bar{1}01]$	0.106	0.25
	critical slip $(\bar{1}11)[101]$	0.272	0.64
$[\bar{2}33]$	primary slip $(111)[\bar{1}01]$	0.371	1
	coplanar slip (111) $[1\bar{1}0]$	0.371	1
	conjugate slip $(\bar{1}\bar{1}1)[011]$	0.223	0.60
	cross slip $(1\bar{1}1)[\bar{1}01]$	0.186	0.50
	critical slip $(\bar{1}11)[101]$	0.148	0.40

a [001] crystal is subjected to straining. However, there are inevitably errors in the orientation of the crystal. The actual stress direction always falls in one of the eight standard triangles adjacent to the [001] pole and, therefore, statistically there is always one among the eight slip systems that has a higher resolved shear stress and would operate first as the primary slip system. In the present study, the most frequently observed slip system to be activated is B4, namely (111) $[\bar{1}01]$. Consequently, the formation of Lomer-Cottrell locks is expected through dislocation reactions between primary slip system B4 and conjugate slip system C1 $((\bar{1}\ \bar{1}\ 1)[011])$. It is rational to say that the higher cyclic hardening rate of [001] crystals is mainly caused by the formation of Lomer-Cottrell locks[23,27]. Unlike [001] crystals, [011] crystals show much lower initial hardening rate $\theta_{0.2}$ which is almost independent with the strain amplitude γ_{pl} (see Fig.2). In Table 2 is listed the four most highly stressed slip systems and the possible dislocation interactions in [011] crystals. Theoretically speaking, B4, B5, A3 and A6 should operate simultaneously. However, only B4 was observed to operate as a primary slip system during cyclic deformation even under higher strain amplitudes and there is no clear indication of the operation of B5, A3 and A6. The strong latent hardening taking place on B5, A3 and A6 might be responsible for the experimental phenomenon. So the initial cyclic hardening of [011] crystals is mainly determined by the primary dislocation multiplication and their interactions[25,28].

Table 2 Four most highly stressed slip systems and probable products of dislocation reactions in [011] crystal

	B4 (111)[$\bar{1}$01]	B5 (111)[$\bar{1}$10]	A3 ($\bar{1}$11)[101]	A6 ($\bar{1}$11)[110]
B4	–			
B5	coplanar dislocations	–		
A3	sessile jogs	Lomer-Cottrell locks	–	
A6	Lomer-Cottrell locks	sessile jogs	coplanar dislocations	–

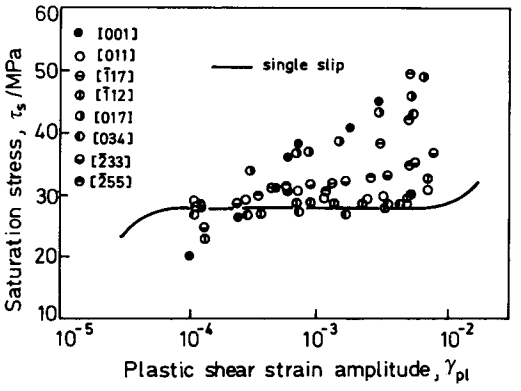

Fig.3 Cyclic stress-strain curves of double- and multiple-slip-oriented Cu single crystals. The solid line represents the results of single-slip-oriented crystals

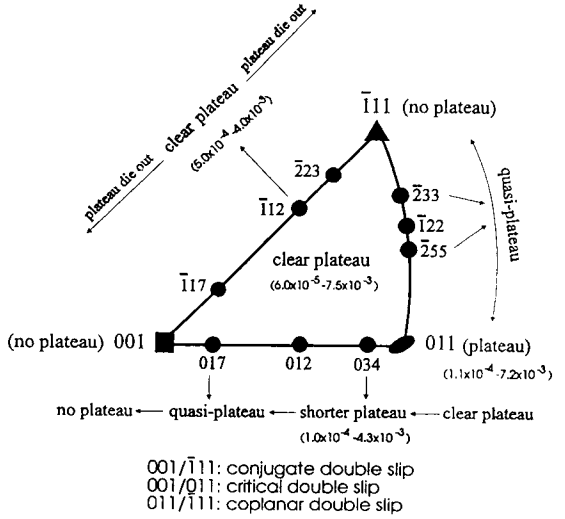

Fig.4 Variation of CSSC with the crystallographic orientation of the crystal

2.3 Effect of crystallographic orientation on CSS curve[22~28]

Unlike the CSS curve of crystals oriented for single slip[15], the CSS curves of double- and multiple-slip-oriented crystals are strongly influenced by their crystallographic orientations, as shown in Fig.3. It can be seen that the orientation of the specimen not only affects the level of cyclic saturation stress, but also the shape of the CSS curve, especially its plateau region. Similar to the $\theta_{0.2}-\gamma_{pl}$ curves in Fig.2, the CSS curves can also be roughly divided into three groups: (1) like the CSS curve for single-slip-oriented crystals, the CSS curve shows a clear plateau, such as crystals [011], [034] and [$\bar{1}$12], (2) there is no clear plateau on the CSS curve, but a quasi-plateau may exist within a certain range of strain amplitude γ_{pl}, such as crystals [$\bar{2}$33] and [$\bar{2}$55], and (3) the saturation stress τ_s increases monotonously with increasing the strain amplitude γ_{pl}. There is no any plateau in the CSS curve, such as crystals [001], [$\bar{1}$17] and [017].

The dependence of CSS curves on the orientation of the specimens can also well be rationalized in terms of the dislocation reactions between different slip systems. [$\bar{2}$23], [$\bar{1}$12] and [$\bar{1}$17] are three conjugate double slip crystals which lie on the 001/$\bar{1}$11 boundary of the standard triangle. Similar to [$\bar{1}$11] crystals[17], [$\bar{2}$23] crystals showed no clear saturation. The CSS curve of [$\bar{1}$12] crystal exhibits a clear plateau which is much shorter than that of the single slip crystals although the saturation shear stresses are nearly the same, while for [$\bar{1}$17] crystals, almost no plateau exhibits on its CSS curve with a much higher saturation stress level. [034] and [017] are two critical double slip crystals which are located closely to [011] and [001], respectively, on the 001/011 boundary. From Fig.3, a plateau can be clearly seen on the CSS curve of [034] crystals, while there is no plateau at all for [017] crystals. [001] and [011] are both multiple-slip-oriented crystals. The data for [001] crystal show apparently no plateau at all. Quite similar to the results reported for Cu polycrystals[13], the cyclic saturation shear stress increases monotonously with increasing shear strain amplitude γ_{pl}. In contrast, it is interesting to note that the CSS curve of [011] crystal shows a clear plateau region over a strain range of 1.1×10^{-4} ~7.2×10^{-3} with an average saturation stress of 29.7 MPa. It must be pointed out that the CSS curve data for [011] crystals follows very closely the CSS curve for single slip crystals, although [011] is a typical orientation for multiple slip.

Based on the experimental data available, a comprehensive diagram as shown in Fig.4 has been worked out to demonstrate the effect of crystallographic orientation on the cyclic stress-strain response. The main points can be summarized as follows: (1) for most orientations within the standard triangle, the shape of the CSS curve appears to be quite constant with a clear plateau regime over a wide strain range,

(2) the CSS curve of [001] and [$\bar{1}$11] crystals shows no plateau, but a clear plateau exists for [011] crystals, (3) [$\bar{1}$12] orientation which shows a clear plateau separates the 001/$\bar{1}$11 boundary into two parts. When the orientation of the specimen varies from [$\bar{1}$12] either towards [$\bar{1}$11] or [001], the plateau regime becomes shorter and finally disappears, (4) On the 011/001 boundary, when the orientation varies from [011] to [001], the shape of the CSS curve changes correspondingly, from one with a longer and clear plateau to one without any plateau with shorter or quasi-plateau in between, (5) On the 011/$\bar{1}$11 boundary, the transition from a clear plateau for [011] crystals to no plateau for [$\bar{1}$11] crystals is characterized by quasi-plateau for [$\bar{2}$55] and [$\bar{2}$33] crystals in-between.

The present study has confirmed that the saturation stress level and the shape of the CSS curve for double and multiple slip crystals are closely related to the orientation of the crystal. The actual result depends on which boundary or summit of the standard triangle lain on. It is reasonable to conclude that if multiple slip in a crystal is a dominant process of cyclic deformation, the CSS curve may show a higher saturation stress level with no plateau regime. Microscopically speaking, the existence or non-existence of a plateau in the CSS curve should certainly be attributed to the effect of the multiple slip behavior associated with the orientation or the dislocation reactions between different slip systems. This conclusion may be helpful in understanding the cyclic deformation behavior of polycrystalline materials.

2.4 Deformation bands induced by cyclic deformation

Besides the general slip bands and the well-known PSBs, an important surface feature defined as deformation bands (DBs) is often seen when the specimen is cyclically strained above a certain strain amplitude in the late stage of cycling. Two types of deformation bands denoted DBI and DBII have been seen in all cyclically deformed crystals in the present study[22~26]. And a third type of deformation bands denoted DBIII was seen for [011] crystals[28]. The crystallographic characteristics of DBI and DBII in differently oriented crystals are quite similar. DBI is almost parallel to the primary slip bands while DBII makes a certain angle with the primary slip bands, as seen in Fig.5(a) and (b), respectively. DBIII can only be seen in deformed [011] crystals and is different from DBI and DBII in its characteristics (see Fig.5(c)).

The habit planes of DBI and DBII for crystals studied in the present work were determined by a simple crystallographic calculation and listed in Table 3. The habit plane of DBI and DBII is closely parallel to the primary slip plane and the conventional kink plane ($\bar{1}$01), respectively. They are not the 45° maximum shear plane as reported by Saletore and Taggart[29], but are perpendicular to each other. A dislocation avalanche mode was first proposed to explain the

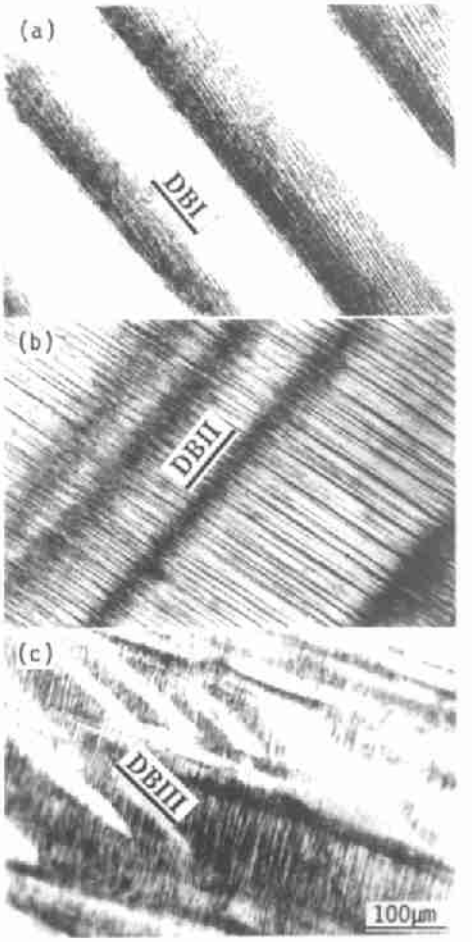

Fig.5 Deformation bands (a) DBI in [$\bar{2}$33] crystal cyclically deformed at $\gamma_{pl} = 3.5 \times 10^{-3}$, (b) DBII in [$\bar{2}$33] crystal cyclically deformed at $\gamma_{pl} = 3.5 \times 10^{-3}$, (c) DBIII in [011] crystal cyclically deformed at $\gamma_{pl}=7.2\times10^{-3}$

formation of DBs during cyclic deformation[30]. Later, we suggested[23] that the poor reversibility of slip may be responsible for the formation of DBs. Recently, Zhai *et al.*[31,32] detected a lattice rotation of about 6° between macrobands and the matrix in cyclically deformed Al single crystals using the time-resolved acoustic microscope. They suggested that this lattice rotation resulted from the accumulation of the irreversible slip in one direction in PSBs and responsible for the formation of these macrobands. In the present work, the rotation of crystal axis during symmetrical push-pull deformation was taken into account to explain the formation of DBs.

It is known from the crystallographic deformation geometry[33] that, during unidirectional tensile tests, a single slip fcc crystal rotates in such a way that the tensile axis approaches to its primary slip direction [$\bar{1}$01], while in unidirectional compressive tests, the stress axis rotates towards the normal to the primary slip plane (111). Therefore, an irreversible rotation

Table 3 Geometrical relationship among DBs, loading axis and some special planes

Loading axis	Habit plane of DBs	Angles between DBI & loading axis	DBII & loading axis	DBIII & loading axis	DBI & (111)	DBII & ($\bar{1}01$)	DBII & ($0\bar{1}1$)	DBII & ($\bar{1}10$)	DBI & DBII
[011]	DBI (0.49 0.67 0.56) DBII (-0.63 -0.18 0.76) DBIII (001)	60°	24°	45°	7°	11°	–	–	90°
[034]	DBI (0.54 0.64 0.56) DBII (-0.59 -0.21 0.78)	56°	30°	–	4°	14°	–	–	89°
[$\bar{2}$55]	DBI (0.70 0.57 0.44) DBII (-0.65 -0.76 0.00)	30°	44°	–	9°	–	–	4°	89°
[$\bar{2}$33]	DBI (0.65 0.57 0.50) DBII (-0.44 -0.25 0.86)	24°	35°	–	7°	23°	–	–	90°
[$\bar{1}$12]	DBI (0.65 0.51 0.57) DBII (-0.64 -0.02 0.77)	24°	59°	–	3°	4°	–	–	89°
[$\bar{2}$23]	DBI (0.59 0.60 0.54) DBII (-0.64 -0.02 0.77)	23°	59°	–	3°	4°	–	–	88°
[$\bar{1}$17]	DBI (0.65 0.60 0.46) DBII (-0.01 -0.63 0.77)	26°	42°	–	12°	–	6°	–	88°

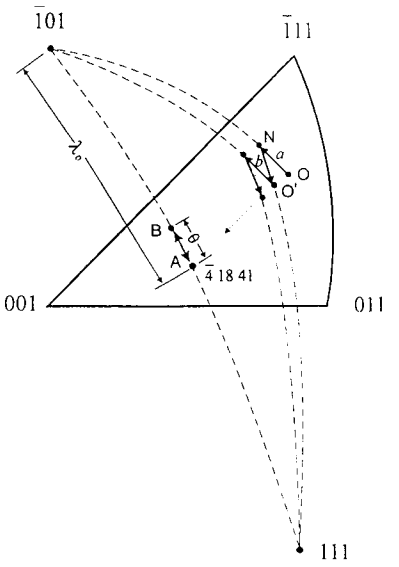

Fig.6 A schematic illustration of the irreversible rotation in a crystal subjected to symmetrical push-pull loading[28]

is expected in the crystal even under symmetrical tension-compression loading. As shown in Fig.6, when a single slip crystal with a stress axis **O** is subjected to tensile loading, the stress axis of the crystal will rotate towards [$\bar{1}$01] along the great circle passing through [$\bar{1}$01] and **O** to **N**. Alternatively, when a compressive loading is followed up, the current stress axis (**N**) of the crystal will move towards [111] from **N** to **O′** along the great circle through **N** and [111]. It is clear that the orientation of the crystal changes irreversibly from **O** to **O′** after one loading cycle. This irreversible rotation will be accumulated with cycling (as indicated by arrow in Fig.6) and may reach a few degree in some local areas, resulting in the observed DBI and DBII.

In view of the analysis above, it is not surprised why DBI and DBII formed along (111) and ($\bar{1}$01), respectively and are perpendicular to each other.

Based on the crystallographic deformation geometry, let us make the following analysis to support the argument above. When a single slip fcc crystal is subjected to unidirectional tension or compression, the corresponding rotational angle towards [$\bar{1}$01] or [111] can be expressed as

$$\sin\lambda_1 = L_0 \sin\lambda_0 / L \tag{1}$$

$$\cos\lambda_2 = L \cos\lambda_0 / L_0 \tag{2}$$

where λ_1 and λ_2 correspond to the angles between the primary slip direction and the stress axis after subjected to tension and compression, respectively. λ_0 is the angle between the initial stress axis and the primary slip direction. L and L_0 are the length of the deformed and undeformed crystals, respectively. Let the stress axis **A** of the crystal situated on the [$\bar{1}$01]-[111] great circular arc rotates to **B** by θ (Fig.6) under tensile loading, then from Eq.(1) we have

$$\sin(\lambda_0 - \theta) = L_0 \sin\lambda_0 / L \tag{3}$$

and

$$L = L_0(1 + \gamma_{\rm pl} \cdot \Omega) \tag{4}$$

where $\gamma_{\rm pl}$ is the applied plastic strain amplitude and Ω is the Schmid factor of the primary slip system. Combining Eqs.(3) and (4), we have

$$\sin(\lambda_0 - \theta) = \sin\lambda_0 / (1 + \gamma_{\rm pl}\Omega) \tag{5}$$

If the stress axis migrates from B back to A along [$\bar{1}$01]-[111] great circular arc under the subsequent compressive loading, similar equations can be derived as follows:

$$\cos\lambda_0 = L \cos(\lambda_0 - \theta) / L_0 \tag{6}$$

$$L = L_0(1 - \gamma_{pl} \cdot \Omega) \quad (7)$$

$$\cos(\lambda_0 - \theta) = \cos\lambda_0(1 - \gamma_{pl}\Omega) \quad (8)$$

Combining formula (5) with (8), we have

$$\sin^2\lambda_0 = (2 - \gamma_{pl}\Omega)(1 + \gamma_{pl}\Omega)^2/4 \quad (9)$$

Since $\gamma_{pl} \cdot \Omega << 1$, therefore

$$\sin^2\lambda_0 \approx 0.5 \Rightarrow \lambda_0 = 45° \quad (10)$$

Apparently, when the stress axis of the crystal is located on the [$\bar{1}$01]-[111] great circle and makes an angle of 45° with both [$\bar{1}$01] and [111], there will be no irreversible rotation and the associated DBI and DBII taking place in the crystal. A [$\bar{4}$ 18 41] crystal which satisfied this orientation requirement was specially prepared and subjected to cyclic deformation. A few DBI and no DBII were observed at strain amplitude as high as 7.7×10^{-3}.

The habit plane of DBIII was determined to be (001). Villechaise *et al.*[34] have observed {100} cubic glide and {100} DBs in the cyclically deformed [$\bar{1}$11] Cu single crystals. The (001) plane in [011] is a maximum shear stress plane because it makes an angle of 45° with the stress axis [011]. This favorable macroscopic state of stress might be responsible for the formation of DBIII in [011] crystal during cyclic deformation[28].

2.5 Dislocation structures and their dependence on crystallographic orientations

The dislocation structure in cyclically deformed Cu single crystals oriented for single slip is well known to strongly depend on the applied amplitude[1,2,4~6]. At plastic shear strain amplitudes (γ_{pl}) over the wide range of the plateau of CSS curve, dislocation configuration consists of ladders and veins which can be described as "two-phase" structure[8,9]. The ladder structure, corresponding to PSBs, is soft and carries most of the applied plastic strain, while the vein structure is hard and contributes little to cyclic deformation. At γ_{pl} below the lower end of the plateau, the dislocation structure consists only of veins. Finally, at γ_{pl} near the upper end of the plateau or beyond the plateau, labyrinth and cell structures associated with multiple slip may develop. However, the dislocation structures of double and multiple slip oriented Cu single crystals produced in fatigue were seldom reported[17~21]. The results of Jin and Winter[19~21] revealed that dislocation configuration of double and multiple slip Cu single crystals depends heavily on their orientations and, hence, on the type of dislocation reactions. However, the above studies were all conducted at only one relatively high strain amplitude ($\gamma_{pl} = 3.0 \times 10^{-3}$) and hence much systematic work is required to understand the micro-mechanisms of cyclic deformation in double and multiple slip oriented crystals.

As examples, the dislocation structures induced by cyclic deformation in [034] and [001] crystals which are double and multiple slip oriented, respectively, are reported below. When the plastic strain amplitude γ_{pl} is less than 1.7×10^{-3}, the dislocation arrangements in cyclically deformed [034] crystals are basically identical. Figure 7(a) and (b) shows a typical example of dislocation structure in the crystal cyclically strained at $\gamma_{pl} = 1.7 \times 10^{-3}$. As the imposed amplitude

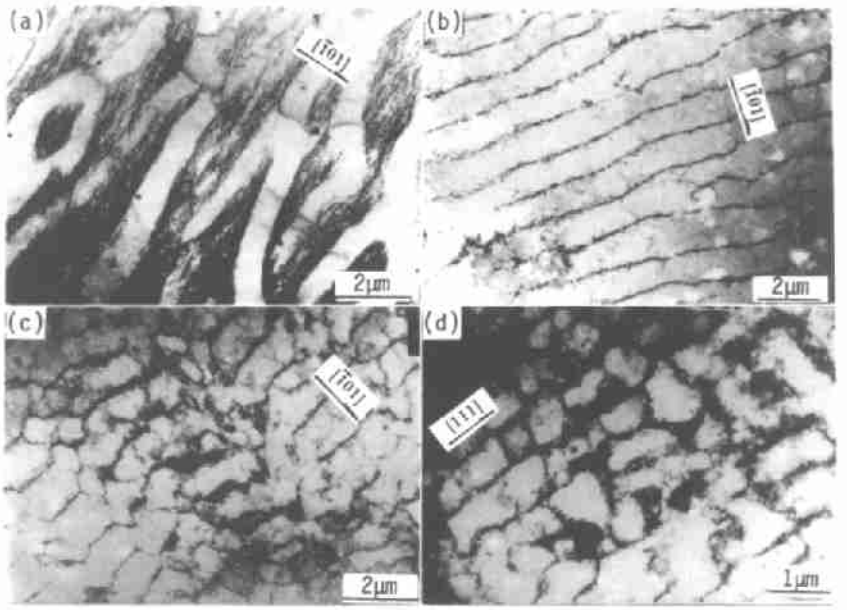

Fig.7 Saturation dislocation structure in a [034] crystal (a) vein structure, (b) wall structure cyclically deformed at $\gamma_{pl} = 1.7\times10^{-3}$, the foil is parallel to the (111) plane, (c) ladder and vein, (d) labyrinth, cyclically deformed at $\gamma_{pl} = 3.4 \times 10^{-3}$

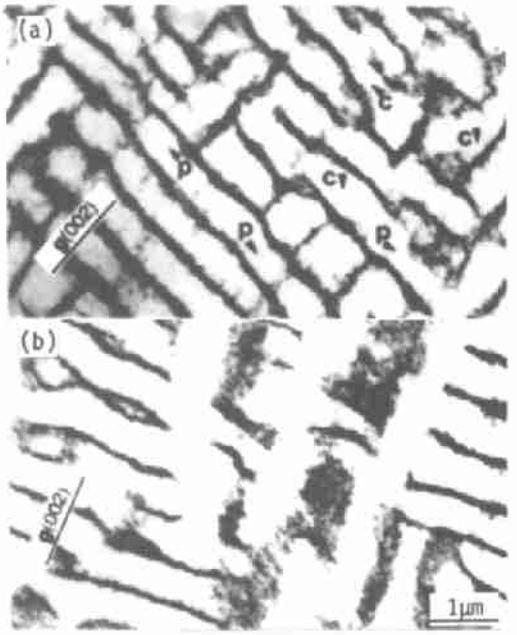

Fig.8 Labyrinth structure in a [001] crystal cyclically deformed at $\gamma_{pl} = 1.8 \times 10^{-3}$ (a) foil is parallel to the $(\bar{1}20)$, **B**=$(\bar{1}20)$ and **g**=(002) and (b) foil is parallel to the (210), **B**=(210) and **g**=(002)

increases to 3.4×10^{-3}, the dislocation arrangements become complicated. The dislocation patterns viewed from a $(1\ \bar{2}\ 1)$ section are shown in Fig.7(c) and (d). Both ladder structures and vein structures can be seen (Fig.7(c)). However, these types of structures occupy only a small fraction of the observed area. The major area is actually covered by labyrinth-type structures, and most of these labyrinth walls are not so condensed (Fig.7(d)). The average width of channels is 0.7 μm, about half of the spacing of the PSB ladders. The observations on dislocation structures in fatigued [034] crystal are in accordance with its cyclic stress-strain response. As compared to that in the single slip crystal, the volume fraction of PSBs in [034] is much less and the labyrinth structure develops at lower strain amplitude due to the involvement of the critical slip, a shorter plateau in the CSS curve of [034] crystal is expected.

In the present study, the dislocation structure of [001] Cu single crystals developed in cyclic deformation over a plastic strain range from 2.4×10^{-4} to 3.0×10^{-3} has been systematically studied[27]. When the specimens were cycled at high strain amplitudes, labyrinth structures containing two perpendicular dislocation walls were frequently observed, as shown in Fig.8. Because one of the labyrinth walls in Fig.8(b) is nearly parallel to the foil plane, *i.e.* (210) plane, several large, "patch-like" walls can be seen in this micrograph. In other words, these patches are actually labyrinth walls parallel to the micrograph. Determination of the geometrical relationship and crystallographic nature of the labyrinth structure was made by extensive observations on various crystallographic plane, such as {210}, $(1\bar{2}1)$, (111) and especially on (001) planes. It was found that one of the two different walls observed was always parallel to the (001) plane; whereas the orientation of the other was changeable, although it is always normal to the (001) plane. Actually, our observation demonstrates that the second type of wall could be one of the following three planes: (100), (210) or (120), with the first two seen more commonly. The nature of dislocation segments in the channels of the labyrinth structures can be directly determined from their geometrical orientations. In Fig.8(a), for example, they have been identified to be screw dislocations with a Burgers vector of $(a/2)[\bar{1}01]$ or $(a/2)[101]$, as marked by "p" and "c", respectively. Figure 9(a) shows the evidence of the bowing out phenomenon of edge dislocations from labyrinth walls into channels. This gives a very similar appearance as in the case of PSB ladder structures in fatigued single crystals with a single slip orientation. The dislocation configuration for intermediate strain amplitudes consists of only homogeneous labyrinth structures. Figure 9 shows the patterns of the labyrinth structures for the case of $\gamma_{pl} = 7.4 \times 10^{-4}$ (Fig.9(b)) and for $\gamma_{pl} = 4.8 \times 10^{-4}$ (Fig.9(c)), where the foil planes are $(1\bar{2}1)$ and $(\bar{1}11)$, respectively. The walls in the labyrinth structures were found to be (001), (100) and (210) walls, similar to those detected in the case of high strain amplitudes. However, the micro-parameters of the labyrinth structure, such as the width of the channel and the volume fraction of the walls, have both been determined to increase obviously with a decrease in strain amplitude. The volume fraction of wall structures for $\gamma_{pl}=4.8\times10^{-4}$ is estimated to be over 50% in comparison with that of about 10% for high strain amplitudes ($1.8\sim3.0\times10^{-3}$). Dislocation structures at low strain amplitudes are found to be basically irregular labyrinth structures, as shown in Fig.9(d). The channels are not as straight as that observed at higher γ_{pl}. In addition, dislocations in the areas between channels are loosely and ununiformly distributed. The width of channels between (001) walls in labyrinth structures formed at various strain amplitudes has been measured on $(\bar{1}20)$ and (210) foils, since they are perpendicular to (001) walls in the labyrinth structure. Results of the measurement are listed in Table 4. It can be seen that the higher the applied strain amplitude, the smaller the channel width and the saturation stress τ_s as well. An attempt was made to estimate the macroscopic flow stress τ based on the bowing out of the edge dislocation from labyrinth walls into channels. As can be seen from Table 4, the calculated results fit the experimental data very well. The dislocation structures observed in the present study are apparently different from the so-called "two-phase" structure observed in single crystal oriented for

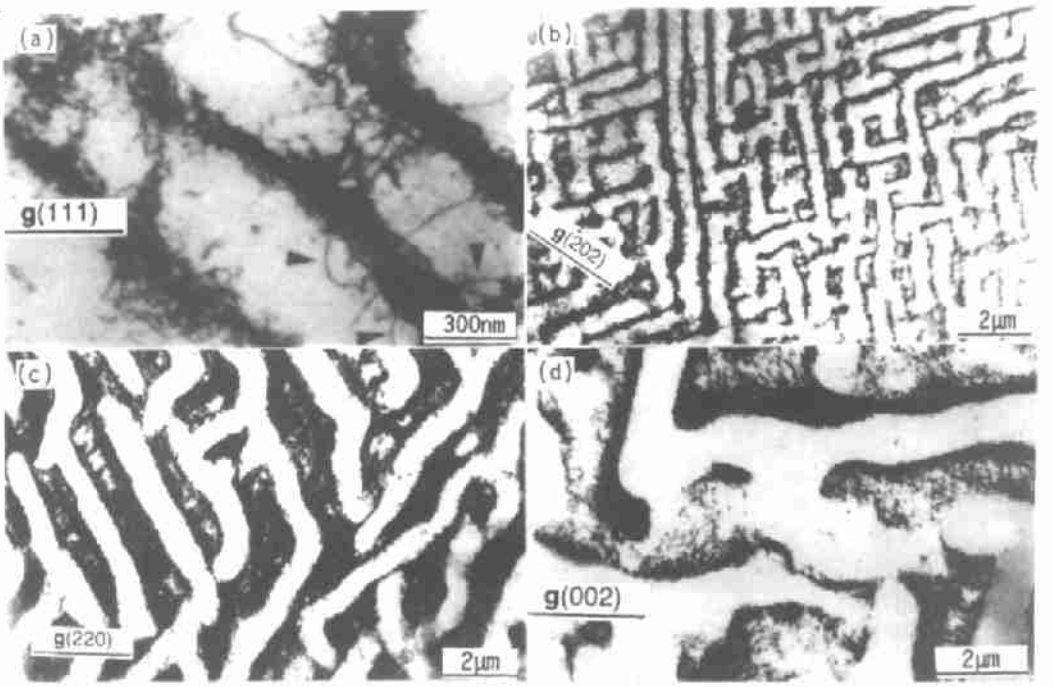

Fig.9 Saturation dislocation structure in a [001] crystal (a) bowing out of edge dislocations from the labyrinth wall (as indicated by arrows) in a [001] crystal cyclically deformed at $\gamma_{pl} = 3 \times 10^{-3}$. The foil is parallel to the (120), **B**=(1 $\bar{2}$ 1) and **g**=(111), (b) labyrinth structure at $\gamma_{pl} = 7.4 \times 10^{-4}$, the foil is parallel to the (1 $\bar{2}$ 1), **B**=(1 $\bar{2}$ 1) and **g**=($\bar{2}$02), (c) $\gamma_{pl} = 4.8 \times 10^{-4}$, the foil is parallel to the (111), **B**=($\bar{1}$11) and **g**=(220). (d) irregular labyrinth structures formed at $\gamma_{pl} = 2.4 \times 10^{-4}$, foils are parallel to the ($\bar{1}$20), **B**=($\bar{1}$20) and **g**=(002)

Table 4 Widths (δ) of labyrinth channels at various γ_{pl} and their relation with saturation stress τ_s

$\gamma_{pl} \times 10^{-4}$	τ_s/MPa	δ/μm	τ/MPa	τ/τ_s
30.0	45.6	0.44±0.03	45.1	0.99
18.0	41.1	0.49±0.07	41.1	1.00
7.2	38.6	0.51±0.04	39.7	1.03
4.8	31.5	0.68±0.07	30.8	0.98
2.4	26.7	0.96±0.09	22.8	0.85

single slip. However, the dislocation structures in fatigued [001] crystals frequently exhibit a large number of similarities to that observed in polycrystals, for example, the labyrinth structures. These similarities certainly result from the multiple slip behavior occurring in cyclic deformation of both materials. It is generally accepted that the formation of PSB ladder structure is the essential reason for the existence of the plateau on the CSS curve. According to the present observations, no PSB ladder structures have been developed in [001] crystals during cyclic deformation. Hence, it is natural to see no plateau in the CSS curve of [001] crystals. Fundamentally, it can be concluded that the existence or non-existence of a plateau on its CSS curve of a certain material depends on whether single slip behavior or multiple slip behavior is predominant during cyclic deformation.

3. Cyclic Deformation and Fatigue Damage Behavior in Cu Bicrystals

The cyclic deformation and fatigue damage behavior of Cu polycrystals has been studied extensively over the past decades[10~14]. However, our knowledge of the cyclic stress-strain response and dislocation structure features in polycrystals is much less as compared to that in single crystals. The cyclic deformation and induced dislocation structures in polycrystalline Cu are affected by many factors, such as grain size, grain boundary (GB) structure, misorientation between grains, strain amplitude, texture and so on. It is established that most of the grains in polycrystals are subjected to double- or multiple-slip and GBs play important role during plastic deformation.

Bicrystals consisting of well-designed component grains can be regarded as good materials for studying cyclic deformation behavior of crystalline materials. In the present work, we have systematically studied the cyclic stress-strain response and the associated dislocation structures of Cu bicrystals with GB either parallel or perpendicular to or tilting at the stress axis[35~42].

3.1 Cyclic stress-strain response of Cu bicrystals

Figure 10 shows the geometries of several fatigue specimens of Cu bicrystal with GB parallel to the

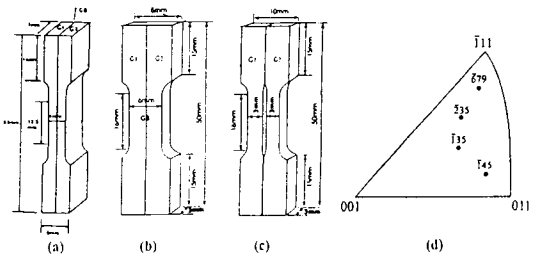

Fig.10 Geometry of fatigue specimens of Cu bicrystals with GB parallel to loading axis (a) [$\bar{1}35$]/[$\bar{1}35$], [$\bar{1}35$]/[$\bar{2}35$] and [$\bar{2}35$]/[$\bar{2}35$], (b) [$\bar{6}79$]/[$\bar{1}45$] (RB), (c) [$\bar{6}79$]/[$\bar{1}45$] (CB), (d) orientations of component crystals

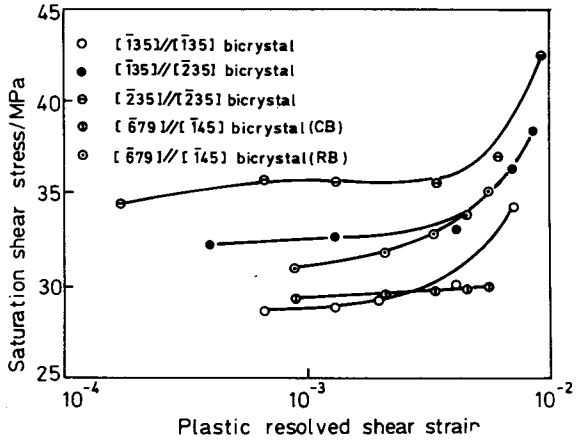

Fig.11 CSSCs of bicrystals [$\bar{1}35$]/[$\bar{1}35$], [$\bar{1}35$]/[$\bar{2}35$] and [$\bar{2}35$]/[$\bar{2}35$] as well as bicrystals [$\bar{6}79$]/[$\bar{1}45$] RB and CB

loading axis. Figure 10(a) is referred to bicrystals [$\bar{1}35$]/[$\bar{1}35$], [$\bar{1}35$]/[$\bar{2}35$] and [$\bar{2}35$]/[$\bar{2}35$], and Fig.10(b) describes a bicrystal [$\bar{6}79$]/[$\bar{1}45$] designed as RB. In order to reveal the effect resulting from GB alone, a combined bicrystal CB was made by simply sticking two individual single crystals [$\bar{6}79$] and [$\bar{1}45$] together at the grip parts. As shown in Fig.10(c), there is no GB in the gauge portion of the bicrystal specimen CB. The crystallographic orientations of all the component crystals in the bicrystals are shown in Fig.10(d), indicating that they are all single-slip-oriented. The CSS curves of bicrystals [$\bar{1}35$]/[$\bar{1}35$], [$\bar{1}35$]/[$\bar{2}35$] and [$\bar{2}35$]/[$\bar{2}35$] as well as bicrystal RB and CB are shown in Fig.11[35,39]. It can be seen that all bicrystals except RB exhibited CSS curves with a plateau region. But the plateau stresses are quite different. For the [$\bar{1}35$]/[$\bar{1}35$] bicrystal and bicrystal CB, their plateau stresses are nearly the same, namely 29~30 MPa, and basically equal to that 28~30 MPa for single-slip-oriented Cu crystals. It is indicated that the strengthening effect of the GB in the coaxial [$\bar{1}35$]/[$\bar{1}35$] bicrystal is negligible. The plateau stresses of bicrystals [$\bar{1}35$]/[$\bar{2}35$] and [$\bar{2}35$]/[$\bar{2}35$] are 32.5 MPa and 36.0 MPa, respectively, and higher than that of single crystals. Since the orientation of [$\bar{2}35$] is close to double-slip, it is believed that the activation of secondary slip owing to the constraint of the GB is responsible for the increase in plateau stress of bicrystals [$\bar{1}35$]/[$\bar{2}35$] and [$\bar{2}35$]/[$\bar{2}35$]. The cyclic saturation stress of the bicrystal RB is higher than that of the bicrystal CB and increases with increasing strain amplitude without showing a plateau region. The difference in cyclic saturation stresses between RB and CB clearly reflected the GB effect on cyclic deformation.

The surface slip morphology of the cyclically deformed bicrystals is quite different from those of the single crystal. As shown in Fig.12(a)~(d), secondary slip was activated in the vicinity of the GB in both bicrystals [$\bar{1}35$]/[$\bar{1}35$] and [$\bar{2}35$]/[$\bar{2}35$]. When the strain amplitude is higher, however, the secondary slip in bicrystal [$\bar{2}35$]/[$\bar{2}35$] was more strong and activated at lower strain amplitude. This observation is nicely in agreement with the CSS behavior of these two bicrystals. Similarly, the secondary slip was also observed near GB in the bicrystal RB, as shown in Fig.12(e). The primary slip lines and secondary slip lines emerged alternately within component crystals [$\bar{1}45$] to form a cross-weaved structure, indicating the GB effect. The width of the GB affected zone increased with increasing strain amplitude. This observation provided a possible explanation on the peculiar cyclic behavior of the bicrystal [$\bar{6}79$]/[$\bar{1}45$] (RB).

In polycrystalline materials, GB orientations with respect to the loading axis are randomly distributed. The deformation distribution within grains across the GB is closely associated with the GB orientation with respect to the loading axis. In order to further understand GB effect on cyclic deformation in polycrystals, it is necessary to study bicrystals with GBs at different angles to the loading axis. Four types of bicrystals with perpendicular GBs [$\bar{3}45$]/[$\bar{1}17$], [$\bar{1}34$]/[$\bar{1}34$], [$\bar{5}913$]/[$\bar{5}79$] and [$\bar{1}23$]/[$\bar{3}35$] were produced for study[36~38,40,41]. In Fig.13(a) are shown the orientations of component crystals in those Cu bicrystals. Lets take the experimental results of bicrystal [$\bar{3}45$]/[$\bar{1}17$] as an example. The cyclic stress-strain curve plotted as axial saturation stress σ_s *vs* axial plastic strain amplitude ε_{pl} is shown in Fig.13(b). The results obtained for small- and large-grained Cu by different authors are also included for comparison. It can be seen that the present bicrystal shows no obvious plateau in the CSS curve, but there is a clear bulge. The curve of the bicrystal is below those of polycrystals. However, when the curves are plotted as shear saturation stress *vs* shear strain amplitude, the CSS curve of the bicrystal is above those polycrystals and close to those of the large-grained Cu[36]. As Fig.13(c) demonstrated, the component crystal orientation of the bicrystal has a strong effect on its cyclic stress-strain response. Bicrystal [$\bar{1}34$]/[$\bar{1}34$] has the

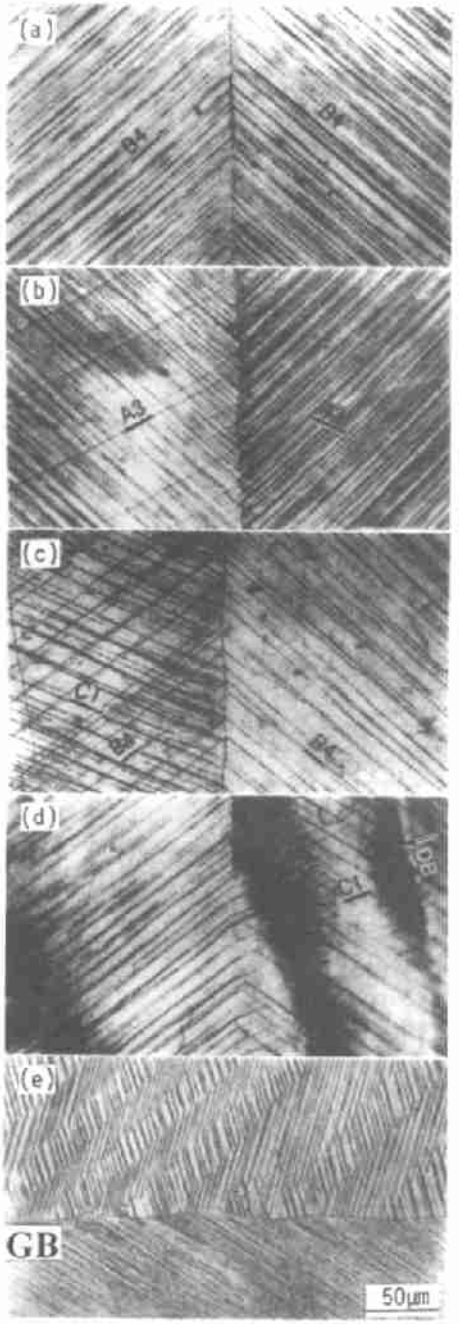

Fig.12 Optical micrographs of slip patterns on the surfaces of Cu bicrystals (a) $[\bar{1}35]/[\bar{1}35]$, $\gamma_{pl} = 6.63 \times 10^{-4}$, (b) $[\bar{1}35]/[\bar{1}35]$, $\gamma_{pl} = 4.08 \times 10^{-3}$, (c) $[\bar{2}35]/[\bar{2}35]$, $\gamma_{pl} = 6.63 \times 10^{-4}$, (d) $[\bar{2}35]/[\bar{2}35]$, $\gamma_{pl} = 6.0 \times 10^{-3}$, (e) $[\bar{6}79]/[\bar{1}45]$ (RB) $\varepsilon_{pl} = 1.5 \times 10^{-3}$

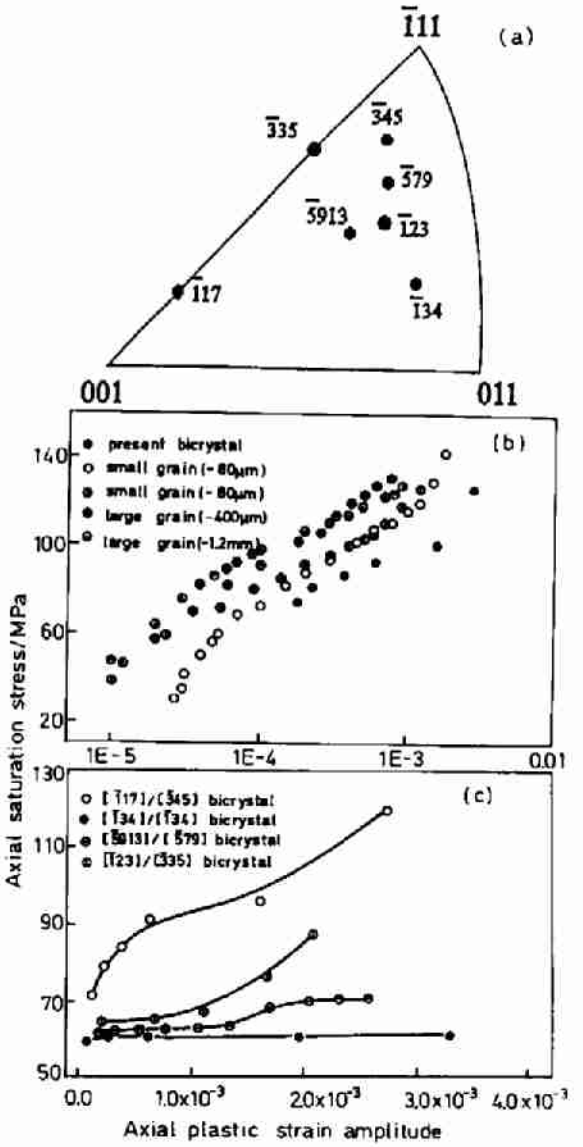

Fig.13 (a) Orientations of component crystals in those Cu bicrystals with a perpendicular GB, (b) CSS curve of $[\bar{3}45]/[\bar{1}17]$ Cu bicrystal and polycrystals, (c) CSS curves of four bicrystals indicating the influence of component crystal orientations

lowest saturation stresses and showed a clear plateau in its CSS curve. As compared to $[\bar{1}34]/[\bar{1}34]$, bicrystal $[\bar{5}913]/[\bar{5}79]$ exhibited higher saturation stresses and two plateau regions in CSS curve. As for bicrystal $[\bar{1}23]/[\bar{3}35]$, the saturation stresses became higher than that of $[\bar{5}913]/[\bar{5}79]$ and there was only a short plateau in the CSS curve. Bicrystal $[\bar{3}45]/[\bar{1}17]$ showed the highest cyclic saturation stresses among the four bicrystals. As mentioned above, the cyclic stress-strain behavior is similar to that of coarse-grained Cu. This systematic variation in the cyclic stress-strain response among the studied four bicrystals can be well explained by the differences in component crystal orientations[40]. Figure 14 schematically illustrates the contribution of each component crystal in a bicrystal to the cyclic stress-strain response and the resulted behavior as a whole.

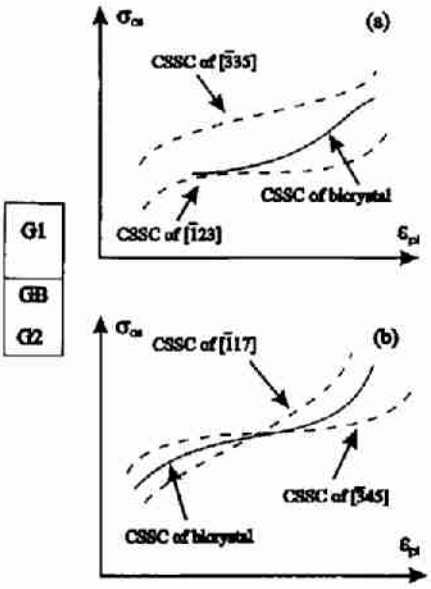

Fig.14 Schematic illustrations of CSS curves of bicrystals consisting of one single- and one double-slip-oriented crystal (a) [1̄23]/[3̄35] bicrystal and (b) [3̄45]/[1̄17] bicrystal

3.2 Interaction of PSBs with GBs and dislocation structures near GBs

GBs with different orientations and structures will act as barriers against slip deformation and act as fatigue crack nucleation sites. These are referred to some localized events, such as the interaction of PSBs with GBs and the local dislocation structures beside GBs, there have been limited reports in this aspect. Recently, the electron channelling contrast (ECC) technique in SEM has been successfully applied to study the dislocation patterns in deformed metals[43~45], such as stainless steel, Ni, Cu and Al. It has been generally recognized that the SEM-ECC technique can reveal some information which is difficultly achieved by conventional TEM technique. For example, it allows the observations of dislocation patterns over the whole cross-section of the specimen, and especially at some special sites, such as the vicinity of GB, deformation bands and crack. Herein, we will mainly discuss the interactions of PSBs with GBs in Cu bicrystals by using the SEM-ECC technique.

Figure 15(a) and (b) present the interaction of PSBs with low-angle GBs during cyclic deformation in a columnar Cu crystal[39]. It is clearly seen that all the PSBs can pass through the GBs continuously without activating any additional slip. Therefore, the stress and strain must be compatible at low-angle GBs which provide no resistance to PSBs. However, when the misorientation of two grains across the GB becomes large, PSBs are unable to pass through GB continuously as shown in Fig.15(c) and (d). By using the SEM-ECC, the cyclically saturated dislocation structure in the vicinity of GB in a Cu bicrystal can be clearly disclosed. Figure 16(a) illustrates the interaction of PSBs with the GB within grain [5̄913] of bicrystal [5̄913]/[5̄79]. In particular, these affected zones developed along a direction other than the primary slip direction of both component crystals[41]. They may be preferential sites for initiating fatigue

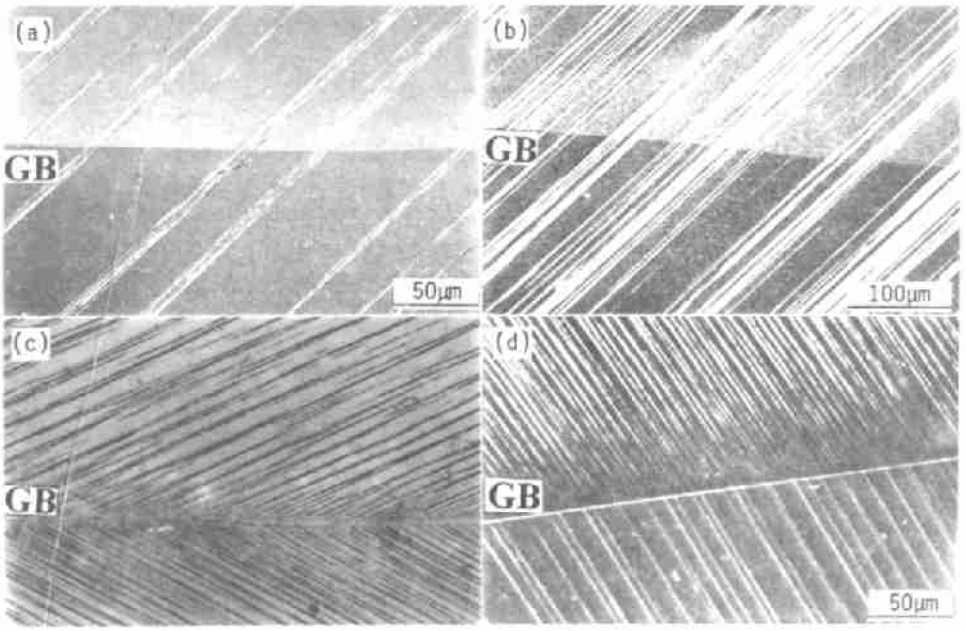

Fig.15 Interactions of PSBs with low-angle GBs at (a) $\gamma_{pl} = 6.4 \times 10^{-4}$, (b) $\gamma_{pl}=3.42\times10^{-4}$. Surface slip patterns around perpendicular GB in bicrystal [5̄913]/[5̄79], (c) viewed from the front surface, (d) viewed from the lateral surface

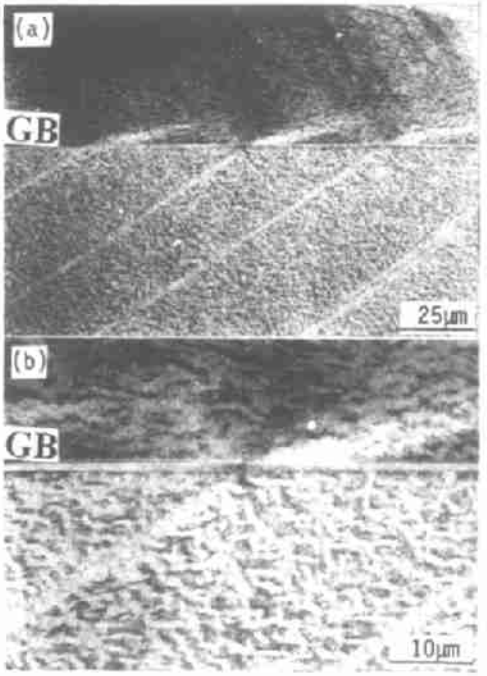

Fig.16 SEM-ECC micrographs showing the interaction of PSB ladder structures with a perpendicular GB in bicrystal [$\bar{5}$913](G1)/[$\bar{5}$79](G2). The bicrystal was cyclically loaded at an axial plastic strain amplitude of 7.6×10^{-4} for 10^4 cycles (a) low magnification and (b) high magnification

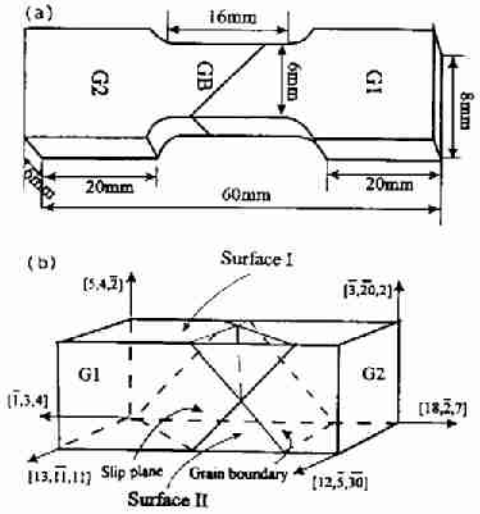

Fig.17 Cu bicrystal [$\bar{1}$34]/[18 $\bar{2}$ 7] with a tilting GB and a common primary slip plane in both component crystals (a) fatigue specimen and (b) crystallographic geometries

cracks although the physical or mechanical properties of these zones need to be further clarified. Furthermore, as shown in Fig.16(b), under higher magnification the ends of PSBs are seen to become sharper and irregular when they approach to the GB, indicating the existence of stress and strain incompatibility

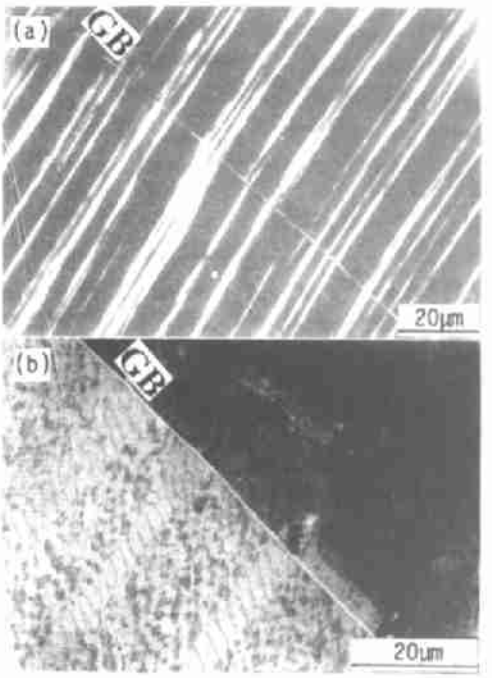

Fig.18 Interactions of PSB with GB in a cyclically strained bicrystal [$\bar{1}$34]/[18 $\bar{2}$ 7] (a) surface slip morphology and (b) SEM-ECC micrograph of dislocation patterns. $\varepsilon_{pl} = 9 \times 10^{-4}$

between the component grains [$\bar{5}$913] and [$\bar{5}$79] during cyclic deformation.

The primary slip planes within grains on both sides of the GB are seldom coplanar. As a natural consequence, slip is often unable to pass through the GB from one grain to another as usually observed. As shown in Fig.17, a special bicrystal with a tilting GB was grown[42]. In this bicrystal, two component crystals G1[$\bar{1}$34] and G2[18 $\bar{2}$ 7] have a common primary slip plane (111). It is expected to observe the continuity of slip lines across the GB in this specially grown bicrystal even though it is a large-angle GB. Figure 18(a) shows the experimental observation which identified that slip can also pass through large-angle GBs continuously if the primary slip planes in the adjacent grains are coplanar. The dislocation structure beneath the surface slip lines was revealed by SEM-ECC technique and shown in Fig.18(b). It is clear that there is no continuity of the PSB ladder structure between component crystals G1 and G2 although the surface slip lines passed though the GB continuously (Fig.18(a)). This is easy to be understood since the observed planes in the grains G1 and G2 are crystallographically different.

Dislocation-free zones (DFZs) beside GBs in fatigued Cu polycrystals were first reported by Winter *et al.*[46]. They found that high angle GBs were frequently associated with zones of 1 μm wide, where dislocation densities were much lower than that in the neighboring matrix structures. Recently, Luoh and

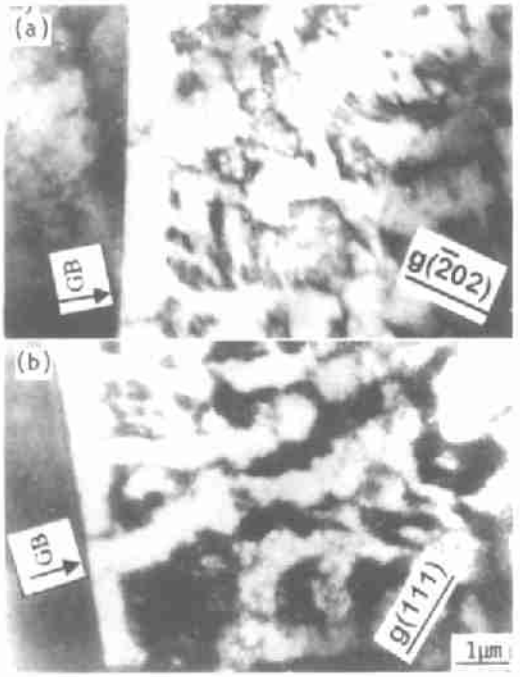

Fig.19 TEM micrographs showing the formation of DFZs in cyclically strained bicrystals (a) [1̄35]/[1̄35], $\gamma_{pl} = 6.63 \times 10^{-4}$ and (b) [2̄35]/[2̄35], $\gamma_{pl} = 6.63 \times 10^{-4}$

Chang[47] claimed based on their investigations that the formation of DFZs in fatigued Cu polycrystals under low plastic strain amplitudes is a very common phenomenon. DFZs beside GBs were also observed in cyclically deformed Cu bicrystals as shown in Fig.19.

Table 5 Values of α and β for the primary slip traces on the surfaces of bicrystal [3̄45]/[1̄17]

Front and back surfaces				Lateral surface			
grain [3̄45]		grain [1̄17]		grain [3̄45]		grain [1̄17]	
α	β	α	β	α	β	α	β
32°	58°	36°	54°	70°	20°	86°	4°

3.3 Fatigue crack initiation along GBs

Crack initiation along GBs in polycrystals of pure metals is often observed under either high-strain or low-strain fatigue. Kim and Laird[48,49] as well as Mughrabi *et al.*[50] developed different models to explain GB fatigue crack initiation. The present work indicates that fatigue crack always initiates at the GB when a Cu bicrystal is cyclically loaded in spite of the GB being parallel, perpendicular to the loading axis, or declined at the loading axis. As an example, Fig.20 shows intergranular cracks induced by cyclic loading in [3̄45]/[1̄17] Cu bicrystal with a perpendicular GB. Generally, these cracks indicated under all the applied strain amplitudes and most of them resulted from the slip bands impingement against GBs. According to the PSB-GB cracking nucleation model[51], if the active Burgers vector in a PSB has a large component parallel to the specimen surface, an intergranular crack can be caused by the stress due to the dislocation piled-up against GB. The cracking stress is associated with geometrical parameters α and β (see Fig.21(a)), where α is the angle between the stress axis and the slip trace, β is the angle between the GB trace and the slip trace[51]. The favorable values are 45° for α and 70.5° for β. In Table 5 are listed the

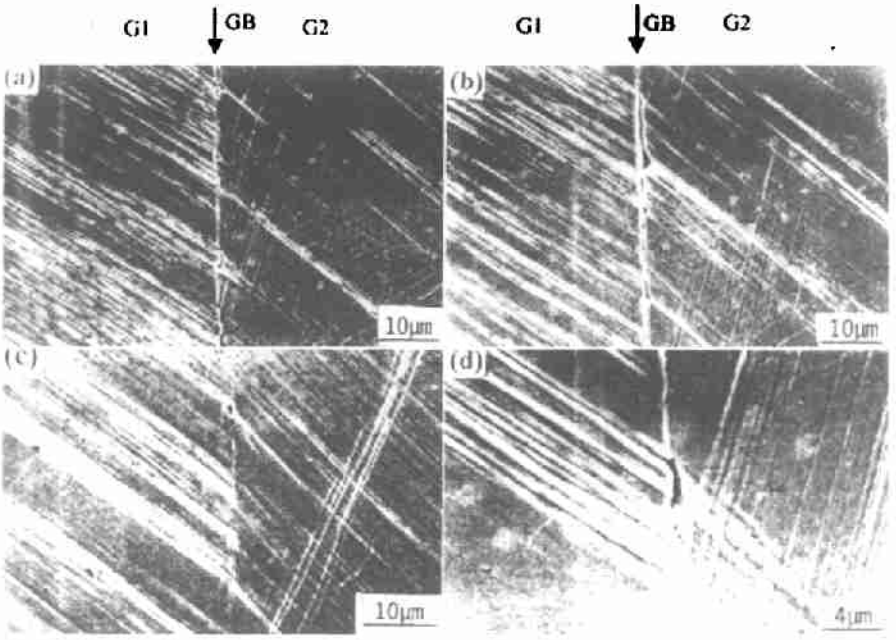

Fig.20 Intergranular cracks induced by cyclic loading in [3̄45]/[1̄17] Cu bicrystal with a perpendicular GB (a) $\gamma_{pl} = 5.4 \times 10^{-4}$, (b) $\gamma_{pl} = 1.63 \times 10^{-3}$, (c) $\gamma_{pl} = 6.45 \times 10^{-3}$, (d) $\gamma_{pl} = 6.45 \times 10^{-3}$

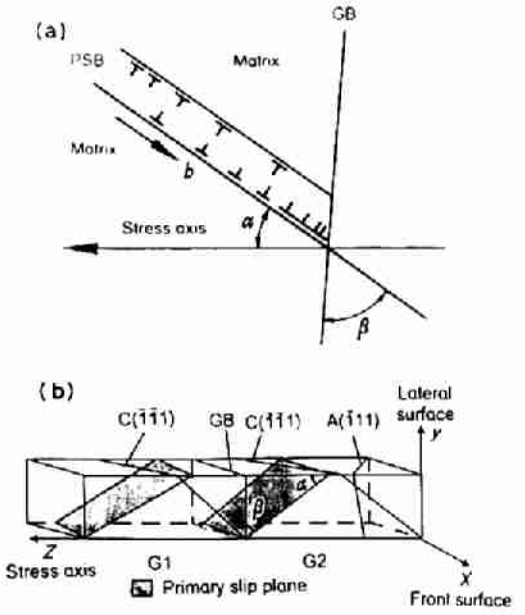

Fig.21 (a) Schematic illustrations of PSBs with GB and stress axis, (b) crystallographic relations of primary slip planes with GB and stress axis in the [3̄45]/[1̄17] Cu bicrystal

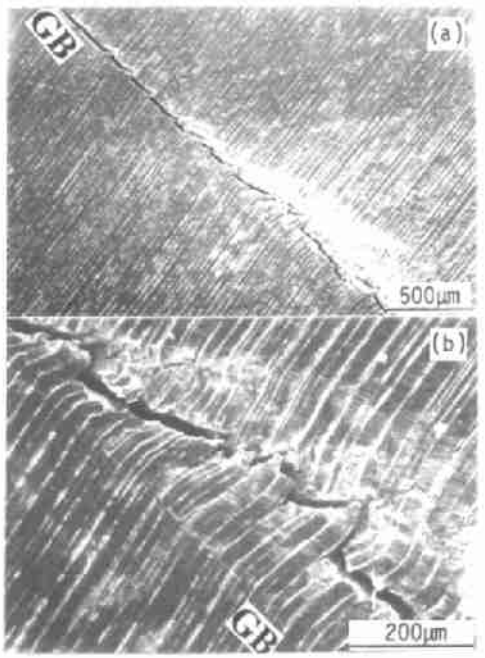

Fig.22 Intergranular fatigue cracking of a [1̄34]/[18 2̄ 7] Cu bicrystal, where the PSBs passed through the GB continuously

values of α and β measured on the front and back surface as well as the lateral surface of the bicrystal specimen [3̄45]/[1̄17] (Fig.21(b)).

It can be seen from Table 5 that the front and back surfaces of the specimen are favorable for crack initiation. The number of fatigue cracks initiated at GB was counted. The result indicates that the crack is more likely to nucleate at GBs on the front and back surfaces. However, PSB-GB model may not explain all the fatigue cracking phenomenon at GBs. For example, intergranular fatigue cracking was also observed in cyclically strained bicrystal [1̄34]/[18 2̄ 7] (see Fig.22(a)) where PSBs passed through the GB continuously without impingement against the GB (see Fig.18). It is also noted under high magnification (see Fig.22(b)) that fatigue cracking is not strictly located at the GB, but deviated from it locally.

4. Cyclic Deformation Behaviors of Cu Tricrystals

Most materials for engineering applications are polycrystals. The GB triple junction (TJ), which exerts an important influence on the structure-sensitive characteristics of polycrystal materials, has been received the least study among lattice defects. Bicrystals, which are regarded as the bridge between monocrystals and polycrystals, can only be used to study the GB effect. The GB triple junction (TJ) occupies a large volume fraction in polycrystals with fine grain sizes. Its role in cyclic deformation should also be noticed. Tricrystal is an ideal material for studying the TJ effect on fatigue process. But owing to the difficulty of crystal growth, only a few investigations have been performed on tricrystals, including some creep tests[52~54] and fatigue crack growth in the vicinity of TJ[55]. In the present study, low cycle fatigue was carried out on Cu tricrystals. The purpose of the present work is to examine the cyclic deformation behavior of tricrystal and the TJ effect on the fatigue damage process. Bicrystal specimens cut from the same crystal were also investigated for comparison.

4.1 Cyclic stress-strain response of Cu tricrystals

A Cu tricrystal ingot was grown from OFHC Cu of 99.999% purity by the Bridgman method. The cross-section of the as-grown tricrystal ingot and the orientations of three grains in the tricrystal are shown in Fig.23(a) and (b), respectively. All three GBs in the tricrystal were identified as random boundaries from a viewpoint of coincidence-site lattice (CSL) model. To study the effects of the boundary node on the cyclic deformation features, a group of tricrystal (TC) and bicrystal (BC) specimens with 14 mm gauge length and 5×7 mm cross-section area were cut from the obtained tricrystal as shown in Fig.23(a). GB.I is oriented perpendicularly to the loading axis. In TC specimen, the boundary node is 2.5 mm apart from the specimen edge along GB.I, half part of the specimen width. Cyclic deformation was carried out on a single tricrystal (TC) and bicrystal (BC) at constant plastic axial strain amplitude in the range of $1\times10^{-4} \le \varepsilon_{pl} \le 4\times10^{-3}$. As shown in Fig.24, the

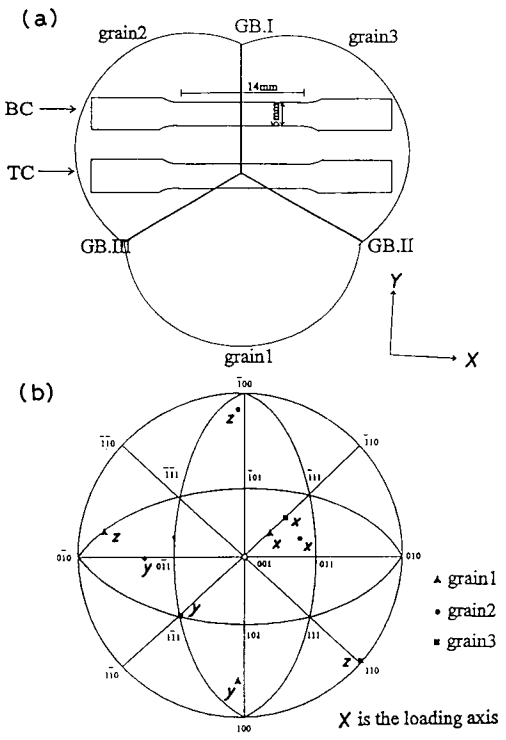

Fig.23 (a) Geometry and dimensions of TC and BC specimens and (b) Stereographic projection of the three grains in the tricrystal

initial cyclic hardening of TC was found to be similar to that of BC at low strain amplitudes. Whereas, the cyclic hardening of TC is higher than that of BC at higher ε_{pl} and the difference becomes pronounced with increasing ε_{pl}. The CSS curve of TC is obviously higher than that of BC (see Fig.25). The axial saturation stresses for TC and BC specimens increased slowly with increasing ε_{pl} and the difference between them is almost independent of ε_{pl} as $\varepsilon_{pl} < 1.5 \times 10^{-3}$. However, the saturation stresses of TC and BC as well as their stress difference increase obviously after $\varepsilon_{pl} > 1.5 \times 10^{-3}$. The present results indicate that the CSS curves of the TC and BC specimens did not exhibit any plateau feature.

4.2 Surface slip characteristics near TJ and GB

The above mechanical behavior is in accord with surface morphologies. The surface morphologies of TC specimens cycled at various strain amplitudes to saturation are shown in Fig.26. At low strain amplitudes, only primary slip system was activated in all three grains, whereas in the vicinity of TJ, the slip traces were retarded, see Fig.26(a). With increasing strain amplitude, both primary and secondary slip systems were activated in the vicinity of TJ in G1 and G3, whereas, no deformation band can be observed, as shown in Fig.26(b) and (c). It is worth noting that at $\varepsilon_{pl} = 2 \times 10^{-3}$ (see Fig.26(d)), microcrack appeared

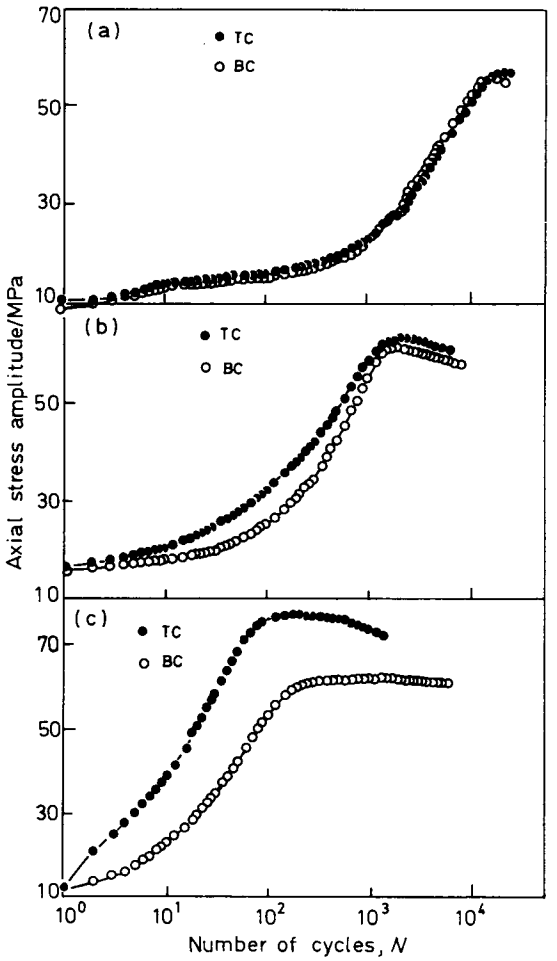

Fig.24 Cyclic hardening curves of TC and BC specimens (a) $\varepsilon_{pl} = 10^{-4}$, (b) $\varepsilon_{pl} = 7 \times 10^{-4}$ and (c) $\varepsilon_{pl} = 2 \times 10^{-3}$

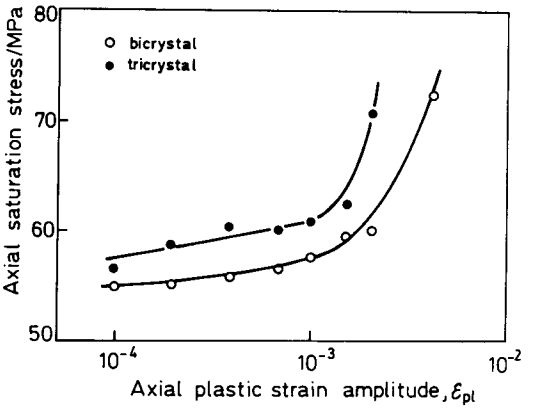

Fig.25 CSS curves of TC and BC specimens

at TJ at low magnification. The surface morphologies of BC specimens cycled at various strain amplitudes to saturation are shown in Fig.27. The secondary slip system was activated near GB even at the lower strain amplitude (see Fig.27(a)). The slip traces became coarser and deeper with increasing ε_{pl}, and at the highest strain amplitude, deformation bands ap-

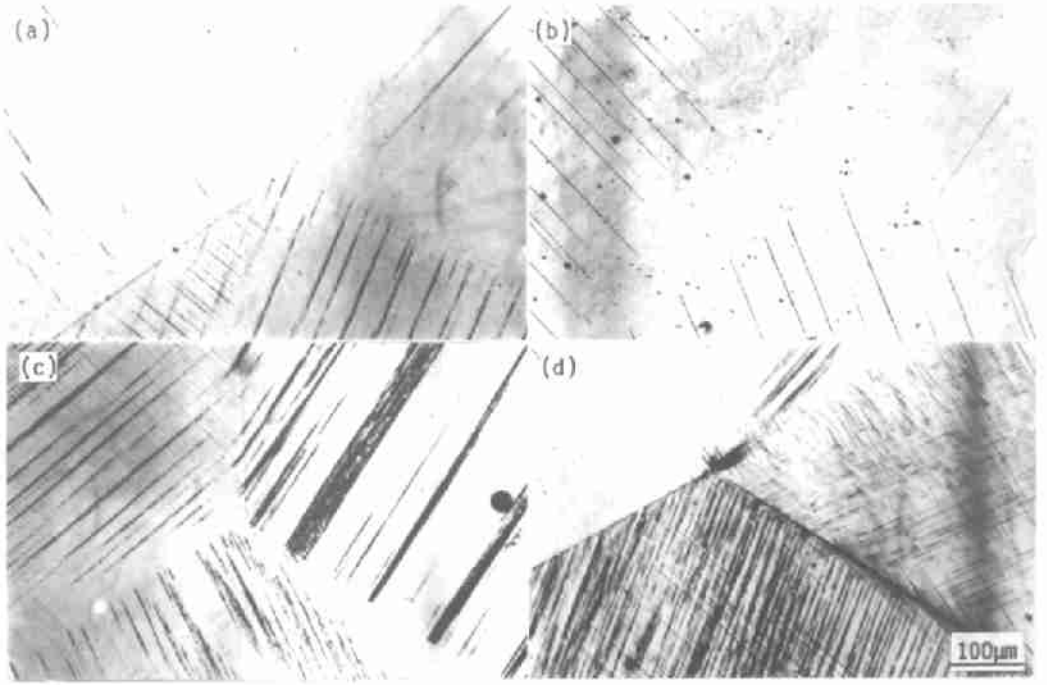

Fig.26 Surface slip morphology of TC specimen under various strain amplitudes (a) $\varepsilon_{pl} = 2 \times 10^{-4}$, (b) $\varepsilon_{pl} = 4 \times 10^{-4}$, (c) $\varepsilon_{pl} = 1.5 \times 10^{-3}$ and (d) $\varepsilon_{pl} = 2 \times 10^{-3}$

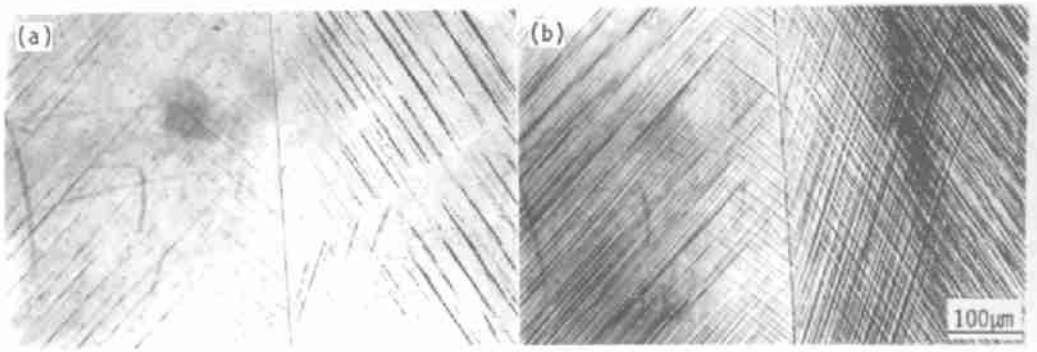

Fig.27 Surface slip morphology of BC specimen under various strain amplitudes (a) $\varepsilon_{pl} = 2 \times 10^{-4}$, (b) $\varepsilon_{pl} = 2 \times 10^{-3}$

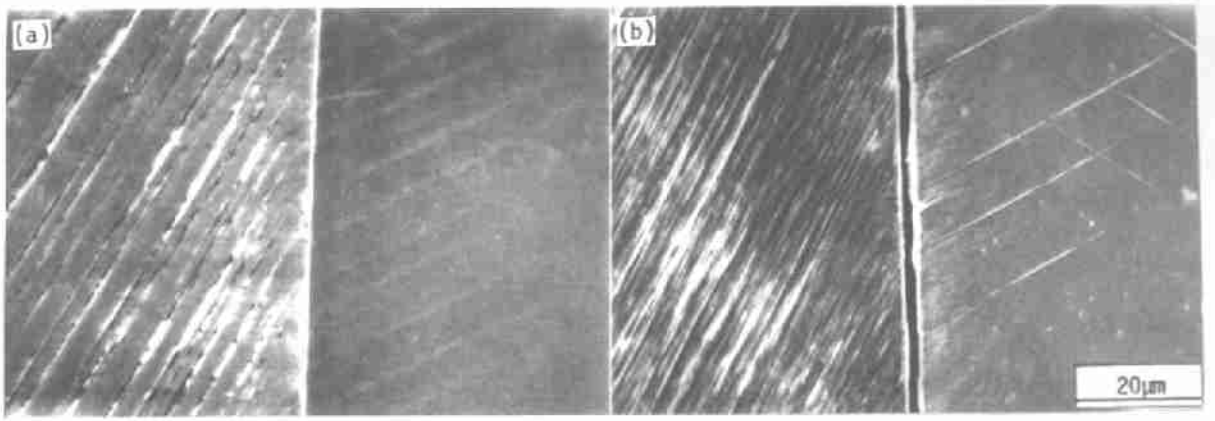

Fig.28 Comparison of surface slip morphology near GB at lateral side between BC and TC specimens (a) $\varepsilon_{pl} = 2 \times 10^{-3}$ TC specimen, (b) $\varepsilon_{pl} = 2 \times 10^{-3}$ BC specimen

peared in the vicinity of GB (Fig.27(b)). In a general view, the deformation degree of BC near GB is larger than that of TC in the vicinity of TJ at the same controlled strain amplitude. Two effects of the GB triple junction (TJ) on slip have been found: one is retardation to the primary slip at lower strain amplitudes; the other is the activation of multiple slip systems due to the internal stresses caused by the strain incompatibilities. Deformation bands appeared near GB for BC at higher strain amplitudes, while they did not occur for TC at the same strain amplitude.

The surface morphologies near GB at lateral side was also observed (Fig.28). It is interesting to note that cracks nucleated along GBs and even GBs were split apart at higher strain amplitudes for BC specimens (Fig.28(b)). While this phenomenon was not observed for TC specimens with the same GB and under the same strain amplitude (Fig.28(a)).

5. Conclusions

(1) The cyclic stress-strain response characteristics of double- or multiple-slip-oriented crystals are closely related to their crystallographic orientations. The existence or non-existence of a plateau on its CSS curve of a certain crystal depends on whether single slip behavior or multiple slip behavior is predominant during cyclic deformation.

(2) Two types of deformation bands denoted as DBI and DBII were investigated in all cyclically deformed crystals in the present work. A third type of deformation bands denoted as DBIII was seen specially for [011] crystals. The habit plane of DBI and DBII are closely parallel to the primary slip plane and the conventional kink plane ($\bar{1}01$), respectively. They are perpendicular to each other. The habit plane of DBIII is (001). The irreversible rotation during symmetrical tension-compression loading is suggested to be responsible for the formation of DBs.

(3) Dislocation configuration induced by cyclic deformation in double and multiple slip Cu single crystals depends heavily on their crystallographic orientations and, hence, on the type of dislocation reactions. The labyrinth structures were frequently observed in [001] crystals with no PSBs ladder structures developed during cyclic deformation. Therefore, it is natural to see no plateau in the CSS curve of the [001] crystals.

(4) Large-angle GBs show strong effect on cyclic deformation and fatigue damage in Cu bicrystals. However, the extent of GBs influence depends on several factors. Among them, the most decisive factors are the orientation of the component crystal and the GB orientation with respect to the loading axis. The two factors will mainly affect the width of GB affected zone and the strain incompatibility within grains. GBs against slip deformation and stopping of PSBs at large-angle GBs are common phenomena in fatigued bicrystals. However, if the two component crystals in a bicrystal have a common primary slip plane, PSBs can also pass through the GB.

(5) Intergranular cracking is often observed in fatigued Cu bicrystals and tricrystals no matter whether the GBs are perpendicular or parallel to the stress axis. The intergranular cracking is associated with the impingement of PSB against GB. In particular, the geometric conditions for intergranular cracking among PSB, GB and stress axis in $[\bar{3}45]/[\bar{1}17]$ bicrystal are in good agreement with those proposed by Christ.

(6) The cyclic hardening rate of TC is higher than that of BC and the difference increases with increasing strain amplitude. The saturation stresses of TC specimens are nearly the same as that of BC specimens at the plastic strain range of $10^{-4} \sim 1.5 \times 10^{-3}$, but are obviously higher than that of BC as the plastic strain amplitude is above 1.5×10^{-3}. At low strain amplitude, primary slip traces are retarded near TJ, while at high strain amplitude, they distribute homogeneously around TJ. Intergranular cracks nucleate easily on the lateral side of BC specimens than that on the lateral side of TC specimens. Macrocracks nucleate near TJ at higher strain amplitudes owing to the accumulation of vacancy generated by annihilation of positive and negative edge dislocations.

Acknowledgement

This work was financially supported by the National Natural Science Foundation of China (NSFC) under Grant No. 19392300-4. The authors are grateful for this support.

REFERENCES

[1] C.Laird: *Dislocations in Solid*, ed. by F.R.N.Nabarro, North Holland, 1983, **6**, 1.
[2] C.Laird: *Physical Metallurgy*, eds by R.W.Cahn and P.Hansen, North Holland, 1996, **3**, 26.
[3] H.Mughrabi: *Fatigue Mechanism, ASTM STP*, 1979, **675**, 69.
[4] Z.B.Basinski and S.J.Basinski: *Prog. Mater. Sci.*, 1992, **36**, 89.
[5] S.Suresh: *Fatigue of Materials*, Cambridge University Press, 1998.
[6] C.Laird, P.Charsley and H.Mughrabi: *Mater. Sci. Eng.*, 1986, **81**, 433.
[7] H.Mughrabi: *Mater. Sci. Eng.*, 1978, **33**, 207.
[8] A.T.Winter: *Philos. Mag.*, 1974, **30**, 719.
[9] J.M.Finney and C.Laird: *Philos. Mag.*, 1975, **31**, 339.
[10] S.P.Bhat and C.Laird: *Scripta Metall.*, 1978, **12**, 687.
[11] H.Mughrabi: *Scripta Metall.*, 1979, **13**, 479.
[12] K.V.Rasmussen and O.B.Pedersen: *Acta Metall.*, 1980, **28**, 1467.
[13] P.Lukas and L.Kunz: *Mater. Sci. Eng.*, 1985, **74**, L1.
[14] C.D.Liu, D.X.You and M.N.Bassim: *Acta Metall. Mater.*, 1994, **42**, 1631.
[15] A.S.Cheng and C.Laird: *Mater. Sci. Eng.*, 1981, **51**, 111.
[16] D.S.Kemsley and M.S.Paterson: *Acta Metall.*, 1960, **8**, 453.

[17] T.K.Lepisto and P.Kettunen: *Mater. Sci. Eng.*, 1986, **83,** 1.
[18] N.Y.Jin: *Philos. Mag.*, 1983, **A48,** L33.
[19] N.Y.Jin: *Philos. Mag. Lett.*, 1987, **A56,** 23.
[20] N.Y.Jin and A.T.Winter: *Acta Metall.*, 1984, **32,** 989.
[21] N.Y.Jin: *Acta Metall.*, 1984, **32,** 1173.
[22] B.Gong, Z.G.Wang and Y.W.Zhang: *Mater. Sci. Eng.*, 1995, **A194,** 171.
[23] B.Gong, Z.R.Wang and Z.G.Wang: *Acta Mater.*, 1997, **45,** 1365.
[24] X.W.Li, Z.G.Wang and S.X.Li: *Mater. Sci. Eng.*, 1999, **A260,** 132.
[25] X.W.Li, Z.G.Wang and S.X.Li: *Mater. Sci. Eng.*, 1999, **A265,** 18.
[26] X.W.Li, Z.G.Wang and S.X.Li: *Mater. Sci. Eng.*, 1999, **A269,** 166.
[27] Z.R.Wang, B.Gong and Z.G.Wang: *Acta Mater.*, 1997, **45,** 1379.
[28] X.W.Li, Z.G.Wang, G.Y.Li, S.D.Wu and S.X.Li: *Acta Mater.*, 1998, **46,** 4497.
[29] M.Saletore and R.Taggart: *Mater. Sci. Eng.*, 1978, **36,** 259.
[30] S.X.Li, B.Gong and Z.G.Wang: *Scripta Metall. Mater.*, 1994, **31,** 1729.
[31] T.Zhai, J.W.Martin, G.A.D.Briggs and A.J.Wilkinson: *Acta Metall. Mater.*, 1995, **43,** 3813.
[32] T.Zhai, J.W.Martin, G.A.D.Briggs and A.J.Wilkinson: *Acta Metall. Mater.*, 1996, **44,** 3477.
[33] C.N.Reid: *Deformation Geometry for Materials Scientists*, Pergamon Press, 1973.
[34] P.Villechaise, J.Mendez and P.Violan: *Acta Metall. Mater.*, 1991, **39,** 1683.
[35] Y.M.Hu, Z.G.Wang and G.Y.Li: *Mater. Sci. Eng.*, 1996, **A208,** 260.
[36] Y.M.Hu and Z.G.Wang: *Acta Mater.*, 1997, **45,** 2655.
[37] Y.M.Hu and Z.G.Wang: *Scripta. Mater.*, 1996, **34,** 1019.
[38] Y.M.Hu and Z.G.Wang: *Int. J. Fatigue*, 1998, **20,** 463.
[39] Z.F.Zhang and Z.G.Wang: *Acta Mater.*, 1998, **46,** 5063.
[40] Z.F.Zhang and Z.G.Wang: *Mater. Sci. Eng.*, 1998, **A255,** 148.
[41] Z.F.Zhang and Z.G.Wang: *Philos. Mag.*, 1999, **A79,** 741.
[42] Z.F.Zhang, Z.G.Wang and H.H.Su: *Philos. Mag. Lett.*, 1999, **79,** 233.
[43] J.Bretschneider, C.Holste and B.Tippelt: *Acta Mater*, 1997, **45,** 3775.
[44] B.Gong, Z.Wang, D.Chen and Z.Wang: *Scripta Mater.*, 1997, **37,** 1605.
[45] A.Schwab, O.Meibner and C.Holste: *Philos. Mag. Lett.*, 1998, **77,** 23.
[46] A.T.Winter, O.B.Pederson and K.V.Rasmussen: *Acta Metall.*, 1981, **29,** 735.
[47] T.Luoh and C.P.Chang: *Acta Mater.*, 1996, **44,** 2683.
[48] W.H.Kim and C.Laird: *Acta Metall.*, 1978, **26,** 777.
[49] W.H.Kim and C.Laird: *Acta Metall.*, 1978, **26,** 789.
[50] H.Mughrabi, F.Ackermann and K.Herz: *ASTM STP*, 1983, **811,** 5.
[51] H-J.Christ: *Mater. Sci. Eng.*, 1989, **A117,** L25.
[52] S.Hashimoto, T.K.Fujii and S.Miura: *Scripta Metall.*, 1987, **21,** 169.
[53] S.Onaka, F.Tajina, S.Hashimoto and S.Miura: *Acta Metall. Mater.*, 1995, **43,** 307.
[54] A.Vinogradov, S.Hashimoto: *Scripta, Mater.*, 1997, **36,** 417.
[55] W.P.Jia, S.X.Li, Z.G.Wang and G.Y.Li: *J. Mater. Sci. Lett.*, 1998, **17,** 1041.